Measurement of the Absolute Luminosity using the Standard Candle $Z \to \mu\mu$ at $\sqrt{s} = 7$ TeV using the CMS Detector

Miles Wu

Advisor: Valerie Halyo

A senior thesis submitted in partial fulfillment of the requirements for the degree of Bachelor of Arts in the Department of Physics at Princeton University

May 2012

Abstract

We perform a measurement of the total integrated luminosity of proton-proton collisions at $\sqrt{s} = 7$ TeV at the Large Hadron Collider (LHC) using $Z \to \mu\mu$ decays. We do this akin to a cross-section measurement, except that we use the theoretical cross-section $\sigma(pp \to ZX) \times \mathcal{B}(Z \to \mu^+\mu^-)$ determined at next-to-next-to-leading-order (NNLO) to solve for the integrated luminosity. We use data taken during 2011 by the Compact Muon Solenoid (CMS) detector, which corresponds to an integrated luminosity of $\int \mathcal{L}dt = 4.638 \pm 0.209$ fb^{-1}, as determined by the official hadronic forward (HF) calorimeter luminosity system. We calculate the integrated luminosity using $Z \to \mu\mu$ decays to be $\int \mathcal{L}dt = 4.718 \pm 0.160$ fb^{-1}; our measurement agrees with the official measurement and has a lower uncertainty.

The stability and consistency of our $Z \to \mu\mu$ decay-based measurement of integrated luminosity, both with respect to time and pileup, are studied. In both aspects we find it to be very stable and agree with official measurements, leading us to recommend its use for future cross-checks on the total integrated luminosity.

Our $Z \to \mu\mu$ decay-based measurement of integrated luminosity is used to leverage the online HF luminosity system, which is the sole online luminosity system at CMS. This is the first time that a physics candle has been used to calibrate this system on the 2011 data and we compare it to the official 2011 HF luminosity calibrated by Van der Meer separation scans.

Measurement of the Absolute Luminosity using the Standard Candle $Z \to \mu\mu$ at $\sqrt{s} = 7$ TeV using the CMS Detector – *Miles Wu*

Acknowledgements

Little did I know when I walked through Valerie Halyo's office door looking for summer research that I would become so enthralled with experimental particle physics. I am indebted to Valerie for the opportunity to get so heavily involved with so many exciting projects in this field, which has, no doubt, led me towards continuing particle physics research at graduate school. Thank you so much Valerie for all your enthusiasm, patience and mentorship, even when you have been unimaginably busy with your recent child and your own work, as I have slowly accustomed myself to research; I will always remember how much you have done for me.

In such a short space of time I have met and collaborated with countless great scientists, but in particular I want to thank Dmitry Bandurin, Sergei Gleyzer, Vasken Hagopian, Adam Hunt, Paul Lujan and Jeremy Werner for always being there to patiently answer my endless questions and to guide me along the precipitous path of research. Without them, none of the research I have done would have been possible.

Studying at Princeton has been a wonderful experience, in part thanks to all the friends I have made and in part thanks to all the dedicated professors across all departments. If I had not had such a delightful time as a student here, I would surely not choose to continue being a student for another five or six years at graduate school, so I thank my friends and all the professors at Princeton.

I would also like to thank all my teachers and fellow students that have given me all the the necessary tools and motivation to study Physics. In particular, I fondly remember my high school physics teacher, Dr. Cullerne, from Winchester College, who encouraged me to always push the boundary of what I thought was possible.

Of course, this work would not be possible without the CMS collaboration and CERN, and their financial supporters. The Large Hadron Collider provides us with the exciting opportunity to find new physics at this new high energy frontier, and as I continue to do particle physics research with the ATLAS collaboration during graduate school, I greatly look forward to this exhilarating period. Even though I will be on a different experiment, my first exposure to particle physics through CMS will not be

forgotten and I believe much of what I have learnt in the last year will remain useful to me for a very long time.

Finally, none of this would be possible without the unconditional support of my parents and I am forever indebted to them. They have always been there to offer advice and to support every decision I've made. I sincerely hope that what I have accomplished in this thesis and at Princeton makes you proud.

Contents

Abstract **i**

Acknowledgements **ii**

Contents **iv**

List of Figures **vi**

List of Tables **viii**

1 Introduction **1**

1.1 Cross-sections and Luminosity 1

1.2 Z Production and Decay 2

1.3 Theoretical Cross-section 3

1.4 Choice of Z Bosons 3

2 Experimental Apparatus **5**

2.1 The Large Hadron Collider 5

2.2 The Compact Muon Solenoid 6

3 HF Luminosity Monitoring **12**

3.1 Hadronic Forward Calorimeters 12

3.2 Offline Methods 14

3.3 Van der Meer Seperation Scans for HF Calibration 15

4 Summer 2011 HF Luminosity Calibration **17**

4.1 Beam Widths 17

4.2 Non-Linearity of the HF 21

4.3 Normalization Change 22

4.4 Motivation for $Z \to \mu\mu$ Measurement 23

5 $Z \to \mu\mu$ Event Selection **25**
5.1 Data and Monte Carlo Samples 25
5.2 Muon Selection Criteria 26
5.3 Software Analysis 29
5.4 Background Processes 29
5.5 Performance Plots 30
5.6 Kinematic Acceptance 31

6 Muon Efficiency and Yield **36**
6.1 Overview of the Tag and Probe Method 37
6.2 Simultaneous Fit using Five Event Categories 37
6.3 Probabilty Density Functions for Signal and Background 39
6.4 χ^2 Goodness of Fit 41
6.5 Results 41

7 Uncertainties in the Measurement **46**
7.1 Statistical Uncertainties 46
7.2 Systematic Uncertainties 46
7.3 Theoretical Uncertainties 47
7.4 Total Uncertainty 48

8 $Z \to \mu\mu$ Integrated Luminosity Measurements **49**
8.1 Trigger Prescaling 49
8.2 Comparison to Van der Meer Scan Calibrated Luminosity 50
8.3 Stability over Time 50
8.4 Stability with regards to Pileup 53
8.5 Cross-check with $Z \to ee$ Decays 55

9 Conclusions **60**

References **61**

List of Figures

1.1 Feynman diagrams for the two dominant Z production processes. 3

2.1 A schematic drawing of the CERN complex and its particle accelerators 6

2.2 A transverse slice of the CMS detector showing the layout of the various sub-detector systems and the paths that different types of particles would take inside the detector. 7

4.1 Van der Meer seperation scans conducted in May 2011. 19

4.2 Van der Meer seperation scans conducted in June 2011. 20

5.1 The track isolation cone around the muon 27

5.2 The event display for a single $Z \to \mu\mu$ decay event 28

5.3 The mass distribution of the $Z \to \mu\mu$ decays observed in data and in our Monte Carlo sample. 31

5.4 The transverse momentum (P_T) distribution of the $Z \to \mu\mu$ decays observed in data and in our Monte Carlo sample. 32

5.5 The η distribution of the $Z \to \mu\mu$ decays observed in data and in our Monte Carlo sample. 32

5.6 The ϕ distribution of the $Z \to \mu\mu$ decays observed in data and in our Monte Carlo sample. 33

5.7 The $\cos(\theta)$ distribution of the $Z \to \mu\mu$ decays observed in data and in our Monte Carlo sample. 33

5.8 The rapidity (y) distribution of the $Z \to \mu\mu$ decays observed in data and in our Monte Carlo sample. 34

6.1 The two signal probablity density functions used for fitting the event categories. 40

6.2 The fit of the $Z_{\mu\mu}^{\mathrm{2HLT}}$ category 42

6.3 The fit of the $Z_{\mu\mu}^{\mathrm{1HLT}}$ category 43

6.4 The fit of the $Z_{\mu s}$ category 44

6.5 The fit of the $Z_{\mu t}$ category 44
6.6 The fit of the $Z_{\mu\mu}^{\text{noniso}}$ category 45

8.1 Calculations of the total integrated luminosity for the 2011 dataset, both from the $Z \to \mu\mu$ method and from the Van der Meer scan calibrated HF system. 51
8.2 Total integrated luminosity for each segment of time-ordered 150 pb^{-1}, as measured by the official Van der Meer scan calibrated HF system. . . 52
8.3 The χ^2/ndof of the simultaneous fit for each segment of time-ordered 150 pb^{-1}, as measured by the official Van der Meer scan calibrated HF system. 53
8.4 The overall efficiency of identifying $Z \to \mu\mu$ decays for each time-ordered segment of 150 pb^{-1}, as measured by the official Van der Meer scan calibrated HF system. 54
8.5 Total integrated luminosity for each instantaneous-luminosity-ordered segment of 150 pb^{-1}, as measured by the official Van der Meer scan calibrated HF system. 56
8.6 The χ^2/ndof of the simultaneous fit for each instantaneous-luminosity-ordered segment of 150 pb^{-1}, as measured by the official Van der Meer scan calibrated HF system. 56
8.7 The overall efficiency of identifying $Z \to \mu\mu$ decays for each instantaneous-luminosity-ordered segment of 150 pb^{-1}, as measured by the official Van der Meer scan calibrated HF system. 57
8.8 The ratio of the integrated luminosity measurement performed using $Z \to \mu\mu$ decays to that using $Z \to ee$ decays for each of the 30 time-ordered segments. 58
8.9 The ratio of the integrated luminosity measurement performed using $Z \to \mu\mu$ decays to that using $Z \to ee$ decays for each of the 30 instanteneous-luminosity-ordered segments. 58

List of Tables

1.1 The main branching fractions for Z boson decay 3

4.1 Effective beam widths calculated for the three Van der Meer scans using the two different methods. 18

4.2 HF non-linearity corrected and uncorrected effective beam widths calculated for the three Van der Meer scans. 22

6.1 The number of events recorded in each event category 38

6.2 The initial and fitted values of the simultaneous χ^2 fit of invariant mass 43

7.1 The uncertainities in our measurement of integrated luminosity. 48

8.1 The initial guesses for the yield used in the simultaneous χ^2 fit for the time-ordered and instantaneous-luminosity-ordered segments 51

Chapter 1

Introduction

1.1 Cross-sections and Luminosity

The cross-section for a given particle interaction is a measurement of the probability that the given interaction occurs. Akin to the classical hard sphere scattering derivation, cross-sections have units of area and for particle physics are typically quoted in units of barns (1 b $\equiv 10^{-28}$ m). Parton-level cross-sections of the process can often be calculated theoretically through quantum electrodynamics (QED) and quantum chromodynamics (QCD). As the Large Hadron Collider (LHC) is a pp collider, each proton in the collision is itself made up of three partons (the quarks). To calculate the overall cross-section, the parton-level cross section is convolved with the two parton probability distribution functions for the proton and this is summed over all the parton pair combinations [1].

Experimentally the the cross-section, σ, is determined by the following relation:

$$\sigma = \frac{\tilde{N}}{\int \mathcal{L} dt}, \tag{1.1}$$

where $\tilde{N}$ is the corrected yield of the given particle(s) and $\int \mathcal{L} dt$ is the total integrated luminosity.

The raw number of observed decay events, N, has to be corrected by three factors to get the corrected yield, $\tilde{N}$, by the following relation:

$$\tilde{N} = \frac{N}{B \times A \times \epsilon}. \tag{1.2}$$

The branching ratio, B, is the fraction for the given particle(s) that decays to the particles we observe and look for in events. The acceptance, A, is the fraction of decay events that we count as decays; this is not 100% because of imperfect geometrical

coverage of the detector and kinematic selection criteria. Finally ϵ is the efficiency of selecting the events due to imperfections in various algorithms and mechanisms.

Luminosity, $\mathcal{L}$, is a measure of the frequency of pp collisions and has units of $\mathrm{cm}^{-2}\mathrm{s}^{-1}$. The total integrated luminosity, $\int \mathcal{L}dt$, is simply the sum of luminosity over time, performed as an integral, which is proportional to the number of pp collisions.

As every production cross-section measurement at the LHC involves $\int \mathcal{L}dt$, the total integrated luminosity, in the divisor, determining the total integrated luminosity to a high degree of accuracy is of large importance. If we solve for $\int \mathcal{L}dt$ in Equation (1.1) and substitute in the yield corrections from Equation (1.2), we find a method for experimentally obtaining the total integrated luminosity:

$$\int \mathcal{L}dt = \frac{N}{\sigma \times B \times A \times \epsilon}. \tag{1.3}$$

In this thesis we perform a measurement of total integrated luminosity delivered to the Compact Muon Solenoid (CMS) at the LHC during 2011, as prescribed by Equation (1.3), using the muonic decay of Z bosons ($pp \to ZX \to \mu^+\mu^- X$). We use our measurement to verify and cross-check the current luminosity system's measurement as our study uses a completely independent method for deriving the measurement.

1.2 Z Production and Decay

There are two main methods for Z boson production at a pp collider, such as the LHC: the first is the leading order (LO) Drell-Yan process and the second is next-to-leading (NLO) quark-gluon scattering. At the LHC, the LO Drell-Yan process accounts for approximately 65% of the total Z boson production, with NLO quark-gluon scattering accounting for most of the remaining 35% [1]. Feynman diagrams for both of these two processes are shown in Figure 1.1, where we have chosen the Z boson to decay into $\mu^+\mu^-$. There are other mechanisms by which Z bosons are produced, but these two processes constitute the vast majority of Z boson production.

Once the Z bosons are produced, they do not live very long; their mean lifetime is a mere $\bar{\tau} = 3 \times 10^{-25}$ s. The dominant branching fractions for Z bosons – what they decay into with what percentage frequency – are listed in Table 1.1. Typically they decay into back into a quark-antiquark pair, but sometimes they decay into a pair of oppositely charged leptons. For our measurement of total integrated luminosity, we are focusing on the muonic decay which occurs only 3.366% of the time [2].

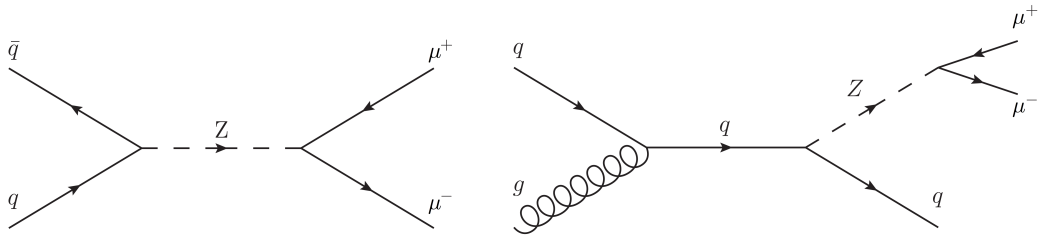

(a) LO Drell-Yan (65%) (b) NLO Quark Gluon Scattering (35%)

Figure 1.1: Feynman diagrams for the two dominant Z production processes.

Decay mode	Branching fraction
e^+e^-	3.363%
$\mu^+\mu^-$	3.366%
$\tau^+\tau^-$	3.367%
$q\bar{q}$	69.91%
$\nu\bar{\nu}$	20.00%

Table 1.1: The main branching fractions for Z boson decay [2].

1.3 Theoretical Cross-section

The theoretical cross-section for Z boson production is calculated at next-to-next-to-leading order (NNLO) using the program FEWZ [3]. The program is given the parton distribution functions from the MSTW08 parton distribution function (PDF) set [4].

As calculated by the program, the cross-section for the invariant mass window that we use ($M \in (60, 120)$ GeV/c^2) at center-of-mass energy $\sqrt{s} = 7$ TeV, including the branching fraction for the muonic decay, is [5]:

$$\sigma(pp \to Z + X) \times \mathcal{B}(Z \to \mu^+\mu^-) = 972 \pm 26 \text{ pb}. \tag{1.4}$$

1.4 Choice of Z Bosons

Z bosons decaying to $\mu^+\mu^-$ were chosen for this total integrated luminosity measurement for a number of reasons:

- The calculation of the theoretical cross-section is well understood at next-to-next-to-leading order.
- The decay has a clean detector signature of two isolated high P_T muons [1]. The main background is QCD multijets which generally does not produce isolated

muons. This allows us to separate signal from background more effectively and obtain a more accurate yield for the luminosity measurement.

- The cross-section of Z boson production, even when it is multiplied by the small branching fraction for muonic decay ($\approx 3.4\%$), is still large enough that copious $Z \to \mu^+\mu^-$ decays are produced [1]. Even after acceptance and efficiency, approximately 300 muonic Z decays are expected in every 1 pb^{-1} of integrated luminosity; at the LHC's design luminosity of 10^{34} $\text{cm}^{-2}\text{s}^{-1}$ this is around 3 $Z \to \mu^+\mu^-$ decays per second. Such a high rate enables a more accurate measurement of total integrated luminosity and perhaps may allow us to monitor the luminosity in near-realtime.

- Measurements of $Z \to \mu^+\mu^-$ decays have already been made for testing electroweak interactions of the Standard Model and for constraining the proton's parton distribution function, so the measurement is well understood [5].

Chapter 2

Experimental Apparatus

This chapter gives a broad overview of the setup of the Large Hadron Collider and the Compact Muon Solenoid detector at CERN. While a detailed description of how the collider and the detector function is not the focus of this thesis, this chapter is intended to familiarize the reader with the basic concepts of how the experiment works in relation to the physics signals we observe in our data.

2.1 The Large Hadron Collider

The Large Hadron Collider (LHC) is a 27 km proton-proton accelerator and collider located at CERN in Geneva, Switzerland, which finished construction in 2008. It was designed to provide a center of mass collision energy of $\sqrt{s} = 14$ TeV at a luminosity of $\mathcal{L} = 10^{34}$ cm^{-2}s^{-1}, but currently it only operates at half that energy and has not quite reached the target design luminosity. This is due to an electric fault that occurred during testing in 2008, which caused a magnet quench that damaged a significant portion of the ring. Although it was repaired in 2009, out of caution the collider will only be operated at $\sqrt{s} = 7$ TeV until the end of 2011. In 2012 it will be run at $\sqrt{s} = 8$ TeV, and at the end of the year it will be shutdown for an extended period of time (approximately two years) to enable various upgrades to be made for operation at the full design energies.

The protons in the LHC are created from ionizing hydrogen gas. These protons are then accelerated by Linac2 to 50 MeV and injected into the PS Booster where they are accelerated to 1.4 GeV. They are then injected into the Proton Synchrotron (PS) which takes them to 25 GeV, and then into the Super Proton Synchrotron (SPS) which accelerates them even more to 450 GeV. Finally they are injected into the LHC's ring where they are slowly taken up to 3.5 TeV over several minutes. The layout of this sequence of accelerators is shown in Figure 2.1, a schematic of the CERN complex.

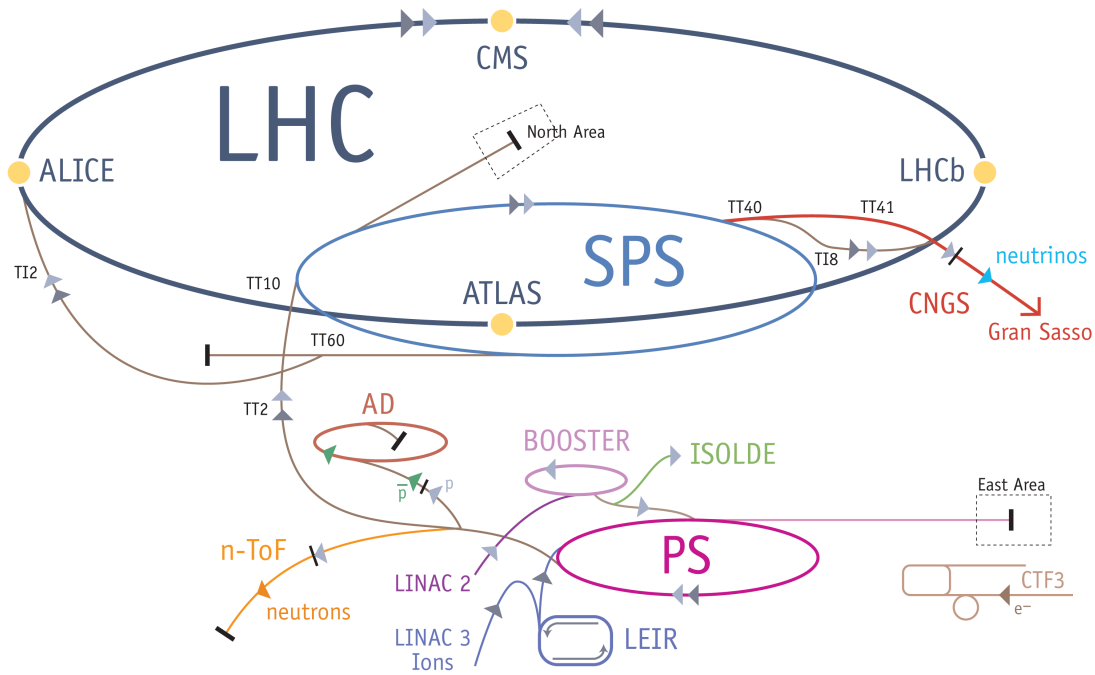

Figure 2.1: A schematic drawing of the CERN complex and its particle accelerators. Experiments other than the LHC are also shown on this diagram. Source: CERN (`http://public.web.cern.ch/public/en/research/AccelComplex-en.html`)

The Tevatron (a proton-antiproton collider in the US) only had a single beampipe as the antiprotons could travel in the opposite direction in the same beampipe due to its negative charge. In contrast, the LHC has two beampipes, one for each proton beam with oppositely directed magnetic fields so that the protons can travel in opposite directions. The magnets in the beampipe are superconducting dipole magnets that can increase the magnetic field in the beampipe up to 8.3 T.

There are currently four detectors situated around the LHC's ring, each situated at an interaction point where the two proton beams cross. Two of these, CMS and ATLAS, are general purpose particle detectors which are fed high luminosity from the collider. The last two, ALICE and LHCb, have more specific purposes and do not receive as much luminosity as the first two.

2.2 The Compact Muon Solenoid

The Compact Muon Solenoid (CMS) is a hermetic particle detector, similar to those used in previous particle physics experiments. It consists of four main sub-detectors,

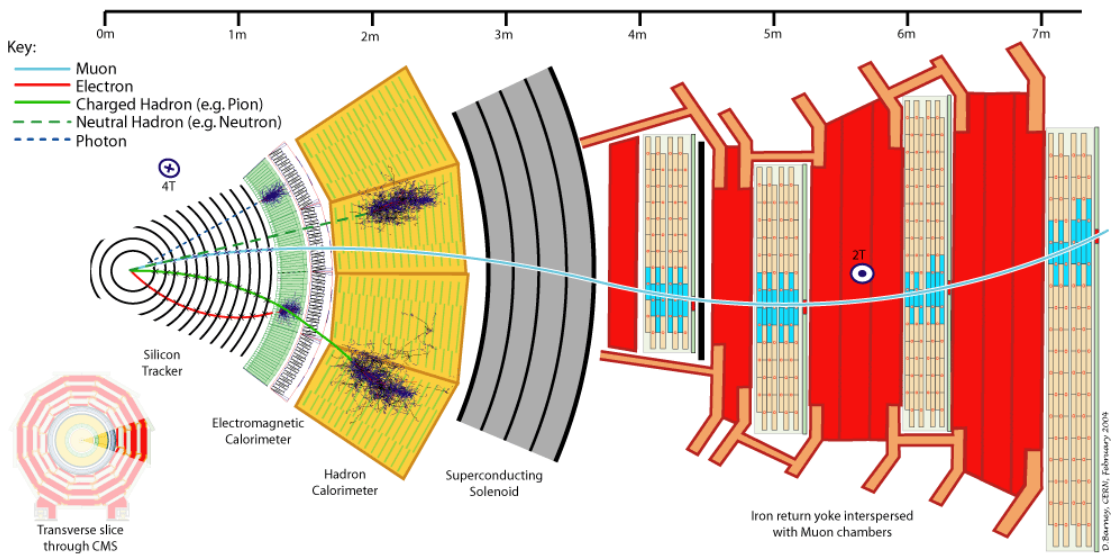

Figure 2.2: A transverse slice of the CMS detector showing the layout of the various sub-detector systems and the tracks that different types of particles would take inside the detector. Source: CMS (`https://cms-docdb.cern.ch/cgi-bin/PublicDocDB/ShowDocument?docid=4172`)

each one surrounding the previous sub-detector like concentric cylinders [6]. Starting from the center of the detector and moving outwards, the four main sub-detectors are: the silicon tracker, the electromagnetic calorimeter, the hadron calorimeter and the muon system. The layout of the detector is shown in Figure 2.2, which is a transverse slice relative to the proton beamline. It also shows the paths that different types of particles would take inside the detector.

We take the beamline to be the direction of the z axis. The azimuthal angle ϕ is therefore the angle in the transverse plane (x-y) and the polar angle θ is the angle to the beamline. We often refer to a quantity known as the pseudorapidity, defined as $\eta \equiv -\ln(\tan(\theta/2))$.

Our measurement of integrated luminosity using $Z \to \mu\mu$ decays relies on muon detection, which concerns the silicon tracker and the muon system. As a result we describe these two sub-detectors in more detail than the two calorimeters.

2.2.1 Superconducting Magnet

A large superconducting solenoidal magnet provides a uniform 3.8 T magnetic field to the free bore of 6 m diameter and 12.5 m length. This large size allows both the silicon tracker and the hadron and electromagnetic calorimeters to reside fully inside

the solenoid magnet. The magnetic field is directed along the z axis and therefore it exerts a force on charged particles that travel transversely, causing their paths to bend. Although the superconducting niobium-titanium coils were originally designed to be able to produce up to a 4 T magnetic field, the magnet is only operated at 3.8 T on the recommendation that it would prolong longevity of the magnet. The magnetic flux is returned through a large iron yoke surrounding the solenoid.

2.2.2 Silicon Tracker

The silicon tracker measures the path taken by charged particles as they bend in the inner magnetic field, because the charged particles cause small ionization currents within the silicon that can be detected and read out by electronics. Muons, electrons and charged hadrons are all detected by it. The silicon tracker surrounds the interaction point (IP) and is 5.6 m in length and 2.5 m in diameter. It consists of two components: the pixel detector and the silicon strip tracker.

The pixel detector contains 65 million silicon pixels, each 100 μm by 150 μm in size, distributed over three cylindrical layers at 4 cm, 7 cm and 11 cm from the beamline and two discs on each end of the barrel. The pixels are this small in order to achieve very high spatial resolution and to keep the occupancies low. Despite the intense particle flux at these close radii, at design luminosities the expected occupancy of each pixel is only approximately 10^{-4} per bunch crossing.

The silicon strip tracker adds another ten cylindrical layers outwards to 1.1 m from the beamline, with twelve discs on each end of the barrel. At these larger radii the particle flux is much lower, allowing silicon micro-strip detectors with a typical size of 10 cm by 80 μm, while still achieving an expected occupancy of a few percent. In total there are 10 million detector strips and the layout of the strips ensures at least nine hits in the pseudorapidity range $|\eta| < 2.4$, ensuring good track reconstruction in this area.

Because of the magnetic field, the direction of the track curvature determines whether the particle is positively or negatively charged and the amount of curvature determines the transverse momentum (higher curvature means lower P_T). The reason for the high magnetic field produced by the superconducting solenoidal magnet is to increase the momentum resolution, especially for high P_T particles, as a larger curvature reduces the uncertainty due to the spatial resolution of the hits. The origin of these tracks are also used to perform vertexing, which is the location of the parent particle's production.

Silicon sensors were chosen to build the tracker, as they have fast response and good spatial resolution and are able to withstand the harsh radiation of the intense particle fluxes. For high transverse momentum tracks such as the ones in our $Z \to \mu\mu$ decays (where $P_T \approx 100$ GeV/c), the transverse momentum resolution of the detector

is approximately 1-2% for $|\eta| < 1.6$ and the transverse impact parameter resolution is approximately 10 μm [1].

2.2.3 Electromagnetic Calorimeter

The electromagnetic calorimeter (ECAL) measures the energy of photons and electrons, by detecting light using photodetectors from scintillations, and the amount of light correlates with the energy of the particle being detected. The ECAL is made up of a barrel section and two endcaps. The barrel section contains 61200 lead tungstate crystals and each endcap section has a further 7324 crystals, together covering the pseudorapidity range $|\eta| < 3$. The photons and electrons are absorbed by the lead tungstate crystals and emit blue-green scintillation light, 80% of which is emitted within the single bunch crossing time at the LHC [1].

2.2.4 Hadron Calorimeter

The hadron calorimeter measures the energy of hadrons and consists of three main sections: the barrel, the endcap and the forward regions. The barrel and the endcap hadron calorimeters are sampling calorimeters that cover the pseudorapidity region $|\eta| < 3$, made with layers of dense brass and steel absorber and 7000 tiles of plastic scintillator. The hadrons are absorbed by the plates of brass and steel, producing secondary particles. These secondary particles then cause scintillations in the adjacent layer of plastic scintillator, which are detected by photodetectors. As with the electromagnetic calorimeter, the amount of light correlates with the energy of the particle being detected.

The forward hadron (HF) calorimeters extend the coverage of the whole hadron calorimeter system up to $|\eta| = 5.2$, making it more hermetic. Because of the intense particle flux in this region, more radiation hard materials are used: quartz fibers are used as the scintillator and these are encased in steel absorber.

2.2.5 Muon System

Muons and neutrinos are the only conventional particles that proceed past the two calorimeters, as they are more weakly interacting. The muon system consists of four layers of muon stations interleaved with the iron return yoke plates in both the barrel region and the two endcaps. The muon stations track the path taken by the muons, similar to the silicon tracker, but, instead of using solid-state silicon, they use gas that is ionized by the muons. Muons can be detected as tracks either in the muon system, or in the silicon tracker, or both.

The muon stations use three different types of muon detectors: muon drift tubes (DTs), cathode strip chambers (CSCs) and resistive plate chambers (RPCs). The barrel region only uses DTs and RPCs and the endcaps only use CSCs and RPCs.

Each layer of muon stations has 60-70 drift chambers, each approximately 2 m by 2.5 m, comprising a total of 172000 muon-sensitive wires. As the DT chambers are only used in the barrel region, this covers pseudo-rapidity range $|\eta| < 1.2$. These drift chambers are used as the track detectors for the muon system in the barrel region.

The endcaps, which is where the rate of muons are the highest, have 468 CSCs that cover the pseudorapidity range $1.2 < |\eta| < 2.4$. In total there are approximately 2 million cathode strip chamber wires and these provide precision muon measurement and triggering. The spatial resolution in r-ϕ is around 75-150 μm.

The RPCs are mainly used for assisting the CSCs in triggering on muons, as while they have excellent time resolution they have poor spatial resolution. In total there are six layers of RPCs in the barrel region and three in the endcaps, covering the pseudorapidity range $|\eta| < 1.6$.

2.2.6 Hermiticity

The detector is hermetic – covering almost all of the 4π solid angle – so that no detectable particles escape without being detected; not only does this avoid missing detectable particles in the collision but it also enables accurate calculation of missing momentum or energy in the collision. Total momentum must sum to zero in a collision, so the missing momentum is simply the difference between the sum of the momenta of the particles detected and the total momentum. The total energy is also known (at the moment it is 7 TeV), so a similar difference yields the missing energy. Neutrinos are so weakly-interacting that they cannot be detected directly; they have to be inferred from the missing momentum and energy. New particles, such as those proposed by supersymmetry theories, are often weakly-interacting and are searched for using this technique.

2.2.7 Trigger

At design luminosity, the LHC will provide approximately 10^9 pp collisions per second, but the detector is only read-out at a frequency of 40 MHz. As a result multiple pp collisions are superimposed on the same event; this phenomenon is known as pileup. The data for a single event is approximately 1 Mb in size, so it is not possible for every single pp collision to be recorded for analysis. Instead, the detector employs a system known as the trigger that only chooses the most interesting events to save. This trigger

is split up into two levels: Level 1 (L1) and Level 3 (L3). The L1 trigger selects the best 100,000 events from the 40 million events that are read-out from the detector by performing simple tests, such as looking for high momenta and energy. Because it only has 25 ms to decide whether to discard the event, the L1 trigger is implemented in dedicated electronics hardware. The L3 trigger uses commodity computers to further reduce the number of events saved per second to 100, utilizing more complex tests like matching inner tracks to hits in the muon system.

Chapter 3

HF Luminosity Monitoring

CMS provides us with the official total integrated luminosity of a given dataset, which we cross check with our measurement using $Z \to \mu\mu$ decays. In this chapter, we describe the method used to obtain this official absolute luminosity measurement using the hadronic forward (HF) calorimeter based relative luminosity measurement.

The number of interactions per bunch crossing is not fixed and is Poisson distributed with mean μ. The mean is:

$$\mu = \sigma(pp \to X)\mathcal{L}\Delta t, \tag{3.1}$$

where $\sigma(pp \to X)$ is the total inelastic proton-proton cross section, $\mathcal{L}$ is the luminosity and Δt is the time between bunch crossings. As the mean is proportional to the luminosity, if we determine the mean number of interactions per bunch crossing we can infer the relative luminosity.

3.1 Hadronic Forward Calorimeters

The forward hadronic (HF) calorimeters (these hadronic calorimeters cover the front end-cap, which is the pseudorapidity range $3 < |\eta| < 5$) can be used to determine the mean number of interactions per bunch crossing, μ, in two different ways.

The first method looks at the occupancy of the HF towers, as the fraction of empty towers can determine the mean number of interactions per bunch crossing, μ, using a technique known as zero counting [1]. Let the number of interactions in a event be the random variable N, which is Poisson distributed with mean μ. For an event that only has a single pp interaction, each HF tower has some probability p of being empty that is independent of all other towers. Therefore, the expected fraction of towers $\langle f_0 \rangle_{N=1}$ that are empty is also p. For an event that has k interactions, the expected fraction of

towers that are empty $\langle f_0 \rangle_{N=k}$ is then p^k. The total expected fraction of empty towers is therefore:

$$\langle f_0 \rangle = \sum_{k=0}^{\infty} \langle f_0 \rangle_{N=k} \; p(N=k) \tag{3.2}$$

$$= \sum_{k=0}^{\infty} p^k \frac{\mu^k e^{-\mu}}{k!} \tag{3.3}$$

$$= e^{-\mu} \sum_{k=0}^{\infty} \frac{(p\mu)^k}{k!} \tag{3.4}$$

$$= e^{\mu(p-1)} = \left(e^{(p-1)}\right)^{\mu}. \tag{3.5}$$

As p is very close to 1, we can take the first-order Taylor expansion of $e^{(p-1)} \approx 1+p-1 = p$.

The expression in Equation (3.5) then simplifies to p^{μ}. If we take the logarithm of this and solve for the mean, μ, we find:

$$\mu \approx \frac{\log\langle f_0 \rangle}{\log p}. \tag{3.6}$$

From the average fraction of empty towers we can calculate the mean number of interactions per bunch crossing. As the value of p differs for different HF rings, we only use a certain subset of HF rings when calculating this.

In practice the technique is not so simple, because the HF towers have noise. To remove the noise, a threshold energy T is introduced, below which a tower is considered empty. However, this changes the form of our equations above. For a single tower, let $n(x)$ be some probability density as a function of energy for noise hits and $s(x)$ be some probability density as a function of energy for actual hits. The probability r_n that a tower is considered empty when there is only noise is therefore $r_n = \int_0^T n(x)dx$ and the probability $r_{s\otimes n}$ that a tower is considered empty when it is actually hit is therefore $r_{s\otimes n} = \int_0^T (s \otimes n)(x)dx$. So long as $(1-p)$ and $(1-p)\mu r_{s\otimes n}$ is small[1] we find [7]:

$$-\log\langle f_0 \rangle = (1-p)\left(1 - \frac{r_{s\otimes n}}{r_n}\right)\mu - \log r_n. \tag{3.7}$$

The average number of interactions per bunch crossing (and therefore the relative luminosity) is now linear with regards to the average fraction of empty towers.

The second method looks at the average total transverse energy deposited per tower, $\langle \sum E_T \rangle$, as this is linear to the mean number of interactions per bunch crossing, μ.

[1] From simulations it was found that these are reasonably small.

Again we let $n(x)$ and $s(x)$ be the probability density functions as a function of energy for the noise and an actual hit respectively. The average energy for a noise hit can then be written as $\nu_n = (\cosh\eta)^{-1}\int xn(x)dx$ and the average energy for an actual hit as $\nu_s = (\cosh\eta)^{-1}\int xs(x)dx$. We find that the average total transverse energy deposited per tower minus some noise constant is proportional to the average number of interactions per bunch crossing (and therefore the relative luminosity) [7]:

$$\langle E_T\rangle = \nu_n + \nu_s(1-p)\mu. \tag{3.8}$$

Although this method has an advantage at high luminosities as it does not require an energy threshold cut (a high μ due to pileup reduces the accuracy of an approximation made in the tower occupancy method) and does not saturate, the tower occupancy method is preferred at the relatively low luminosities delivered by the LHC so far as it has better performance.

Both methods developed by Valerie Halyo and her group [7] are able to measure the mean number of interactions per bunch crossing in real time, which is useful for detector and LHC operations (the stability of the bunch structure and the impact of noise, such as beam gas, on the luminosity can be observed in real time). However, at the moment using the tower occupancies of the hadronic forward calorimeters is the primary method used to determine the mean number of interactions per bunch crossing, μ.

3.2 Offline Methods

There are additional methods used to calculate the relative luminosity that can be done by analyzing data offline [8], such as the pixel luminosity, which uses pixel cluster counting as a number proportional to the luminosity. These work similarly to the online zero counting method, in that the number of empty bunch crossings is counted and μ inferred. Typically these are available around 24 hours after the run has ended, so there is some lag before the luminosity can be calculated using these methods. As these are primarily used as a cross check on the HF measurement, we will not delve into their details.

While we may have sufficient $Z \to \mu\mu$ decays to do our measurement of integrated luminosity to an accuracy of a few percent with less than an hour of data from a run, it is worth noting that we need the data to be processed and reconstructed before we can analyze it and calculate our measurement. This means that our measurement of integrated luminosity using $Z \to \mu\mu$ decays will have approximately the same amount of delay as the current offline methods.

3.3 Van der Meer Seperation Scans for HF Calibration

Equation (3.1) states that the luminosity $\mathcal{L}$ is directly proportional to the mean number of interactions per bunch crossing μ, which we measure using the HF calorimeters. To obtain the luminosity, we could substitute in a value for the proton-proton cross-section $\sigma(pp \to X)$ and the time between bunch crossings $\Delta t = 25$ ns and solve for $\mathcal{L}$. However, this is not done because Van der Meer separation scans allow us to determine the absolute luminosity with a lower uncertainty [9]. In these scans, the event rate as a function of beam displacement (the offset between the two colliding beams) is measured and this information allows us to obtain the effective area of the beam. The measurements are obtained by sweeping one beam in steps across the other beam in first the x direction and then the y direction independently.

Recall that the absolute luminosity is defined as the particle flux, that is, the number of particles per unit area per unit time. For the a ring collider, like the LHC, we can express the peak luminosity $\mathcal{L}$ (when the beams are aligned) as

$$\mathcal{L} = \frac{N_1 N_2 N_b f}{A_{\text{eff}}}, \tag{3.9}$$

where N_1 is the number of particles in each bunch in the first beam, N_2 is the number of particles in each bunch in the second beam, N_b is the number of bunches that collide, f is the frequency of collision and A_{eff} is the effective transverse area of the beam. The number of particles in each bunch of the beam is known by measuring the beam current using Fast Beam Current Transformers (FBCTs) and the time between collisions is known too, so only the transverse area of the beam is not known.

Let the normalized particle density of the beam (the beam profile) be the product of an independent distribution in each x and y direction: $F(x, y) = F_x(x)F_y(y)$, where both F_x and F_y are normalized. We can adapt Equation (3.9) to be the luminosity as a function of beam separation simply by adding the beam profile as a factor:

$$\mathcal{L}(\Delta x, \Delta y) = \frac{N_1 N_2 N_b f}{A_{\text{eff}}} F(\Delta x, \Delta y). \tag{3.10}$$

The effective area A_{eff} can also be written as:

$$A_{\text{eff}} = \frac{\int F(\Delta x, 0) d\Delta x \int F(0, \Delta y) d\Delta y}{F(0, 0)}. \tag{3.11}$$

Putting these two together, we obtain:

$$\mathcal{L}(\Delta x, \Delta y) = \frac{N_1 N_2 N_b f F(0,0)}{\int F(\Delta x, 0) d\Delta x \int F(0, \Delta y) d\Delta y} F(\Delta x, \Delta y). \tag{3.12}$$

While the beam is mostly Gaussian (the core has a Gaussian shape and contributes most of the luminosity), it has been observed that there are non-gaussian components to the beam, especially in the tails [8]. Out of convenience, the beam has been modelled as the sum of two gaussians, leading to:

$$F_u(d) = \frac{h_u}{\sqrt{2\pi}\sigma_{1u}} e^{\frac{-d^2}{2\sigma_{1u}^2}} + \frac{1-h_u}{\sqrt{2\pi}\sigma_{2u}} e^{\frac{-d^2}{2\sigma_{2u}^2}}, \tag{3.13}$$

where u is either x or y and d is the beam separation in the u plane..

Substituting these into Equation (3.12), we find the following as an expression for the luminosity as a function of the beam separation in the u plane:

$$\mathcal{L}(d) = \mathcal{L}_0 \left(\frac{h_u}{\sqrt{2\pi}\sigma_{1u}} e^{\frac{-d^2}{2\sigma_{1u}^2}} + \frac{1-h_u}{\sqrt{2\pi}\sigma_{2u}} e^{\frac{-d^2}{2\sigma_{2u}^2}} \right), \tag{3.14}$$

where

$$\mathcal{L}_0 = \frac{N_1 N_2 N_b f}{2\pi \sigma_{\text{eff-x}} \sigma_{\text{eff-y}}} \tag{3.15}$$

$$\text{and} \qquad \sigma_{\text{eff-u}} = \frac{\sigma_{1u}\sigma_{2u}}{h_u \sigma_{2u} + (1-h_u)\sigma_{1u}}. \tag{3.16}$$

The measurements from the Van der Meer scans are then fitted using Equation (3.14) and thus this yields the absolute luminosity. As this method of obtaining the absolute luminosity does not rely on any theoretical results and is completely experimentally driven, it is currently the preferred method for calibrating the luminosity.

Chapter 4

Summer 2011 HF Luminosity Calibration

The absolute calibration of the luminosity is done every year and here we show our work on the 2011 luminosity calibration. While the 2011 luminosity calibration is not directly relevant to our measurement of integrated luminosity using $Z \to \mu\mu$ decays, the calibration study reveals several weaknesses in the official Van der Meer scan calibrated HF luminosity measurement that motives us to do our measurement using an independent method for cross-check purposes.

4.1 Beam Widths

There were three Van der Meer separation scans conducted in 2011 at CMS: two in May and another in June. Using these scans we calculate the effective width of the beam, $\sigma_{\text{eff-x}}$ and $\sigma_{\text{eff-y}}$, by fitting the sum of two gaussians, as in Equation (3.14), in RooFit[1] to the luminosity profile as the beam separation in one plane was varied. The relative luminosity profile was measured by the HF calorimeters using the tower occupancy method (see Section 3.1). For each scan this one was done in both the x and y direction.

Figure 4.1 and Figure 4.2 show for each scan both the luminosity profile as the beam separation was varied and our double gaussian fit to it. The red and green lines each represent one of the gaussians, while the blue lines are the sum of the two gaussians. The black points are the data to which we are fitting. The fit parameters and the calculated effective sigma are also shown on the plots, in units of mm. The reduced χ^2 for all the six fits are reasonable, and most of this fitting error comes from fitting the

[1] RooFit is a software toolkit that can be used to perform likelihood fits.

Scan	Method	$\sigma_{\text{eff-x}}$ (mm)	$\sigma_{\text{eff-y}}$ (mm)
May Scan 1	OCC	0.05796 ± 0.00005	0.05590 ± 0.00007
	$\sum E_T$	0.05805 ± 0.00005	0.05598 ± 0.00008
	Ratio	1.0016 ± 0.0012	1.0014 ± 0.0019
May Scan 2	OCC	0.05862 ± 0.00006	0.05629 ± 0.00008
	$\sum E_T$	0.05870 ± 0.00006	0.05637 ± 0.00009
	Ratio	1.0014 ± 0.0014	1.0014 ± 0.0021
June Scan	OCC	0.04920 ± 0.00003	0.04473 ± 0.00002
	$\sum E_T$	0.04948 ± 0.00003	0.04505 ± 0.00002
	Ratio	1.0057 ± 0.0009	1.0072 ± 0.0006

Table 4.1: Effective beam widths calculated for the three Van der Meer scans using the two different methods. No length-scale or non-linearity corrections have been applied. Ratios of the beam width calculated by the $\sum E_T$ method to the beam width calculated by the tower occupancy method (OCC) have also been calculated.

non-gaussian tail regions. The statistical uncertainty in σ_{eff} is of the order of a tenth of a percent, which is extremely good.

Effective beam widths were also calculated using relative luminosity data from the $\sum E_T$ method of the HF calorimeters (see Section 3.1) and compared to the usual tower occupancy method in Table 4.1. In the two May scans, the two methods agree on the beam width to within less than 0.2%, approximately within the statistical uncertainties of the fitting. In the June scan, the two methods agree to within less than 0.8%, which is still excellent agreement. Cross-checking the effective beam widths with both methods indicates that the calculated values are consistent and reliable.

The effective beam widths, σ_{eff}, were determined from Δx and Δy, the beam separation distances. However, these distances are determined by the calibration of the magnets that are used to direct the beams. A better distance measurement can be done by using the highly accurate inner silicon tracker: the beamspot is moved by moving both beams by the a given offset, as measured by the magnets, and the beam offset measured using the vertex detector. The ratio of the offsets is the correction, which is known as length-scale calibration.

In the May scan, length-scale scans were performed and the corrections were found to be [10]:

$$\begin{aligned} \frac{\Delta x_{\text{vtx}}}{\Delta x_{\text{magnet}}} &= 0.993 \pm 0.002, \\ \frac{\Delta y_{\text{vtx}}}{\Delta y_{\text{magnet}}} &= 0.992 \pm 0.002. \end{aligned} \tag{4.1}$$

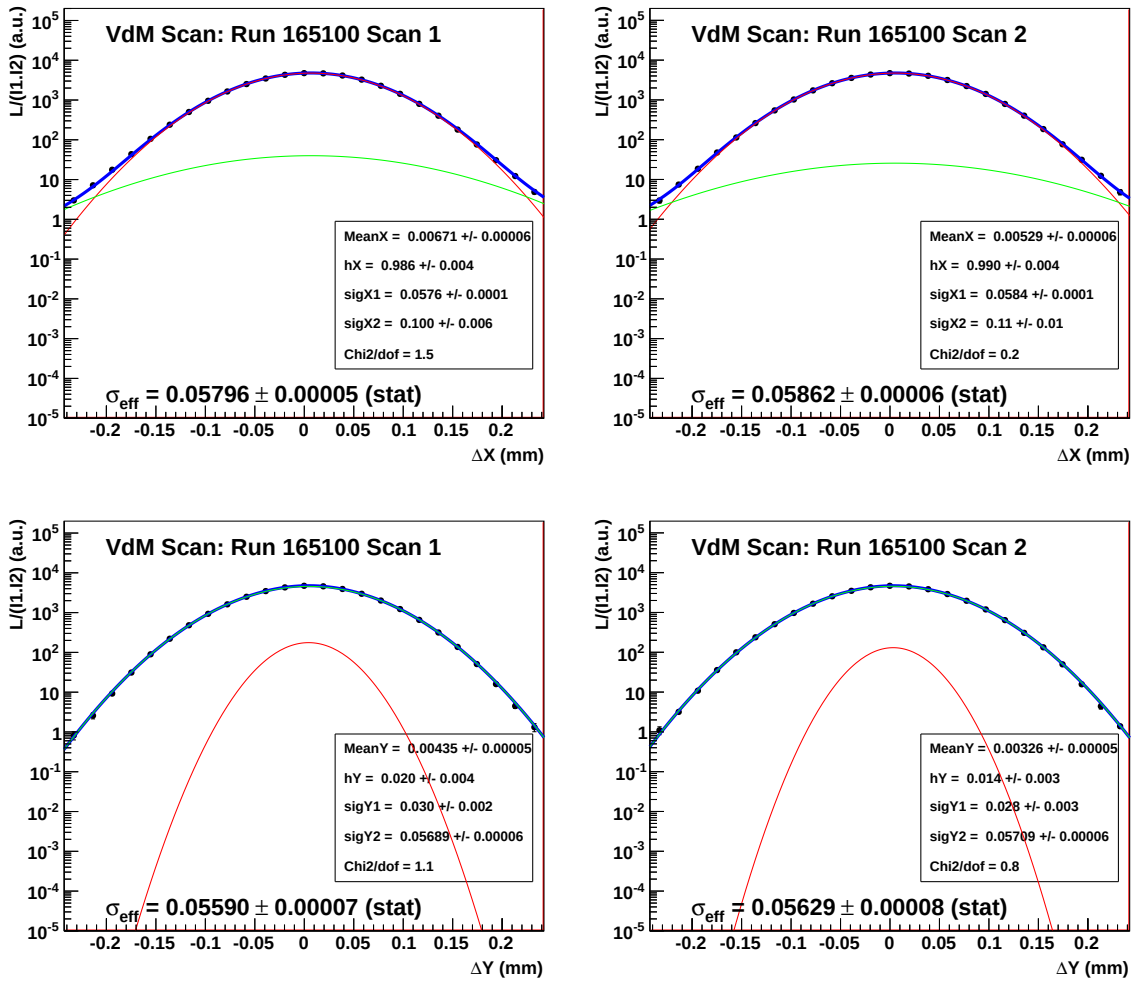

(a) Scan 1 (b) Scan 2

Figure 4.1: Van der Meer seperation scans conducted in May 2011, using the tower occupancy method. The fit parameters and the effective sigma are listed on the plots in mm.

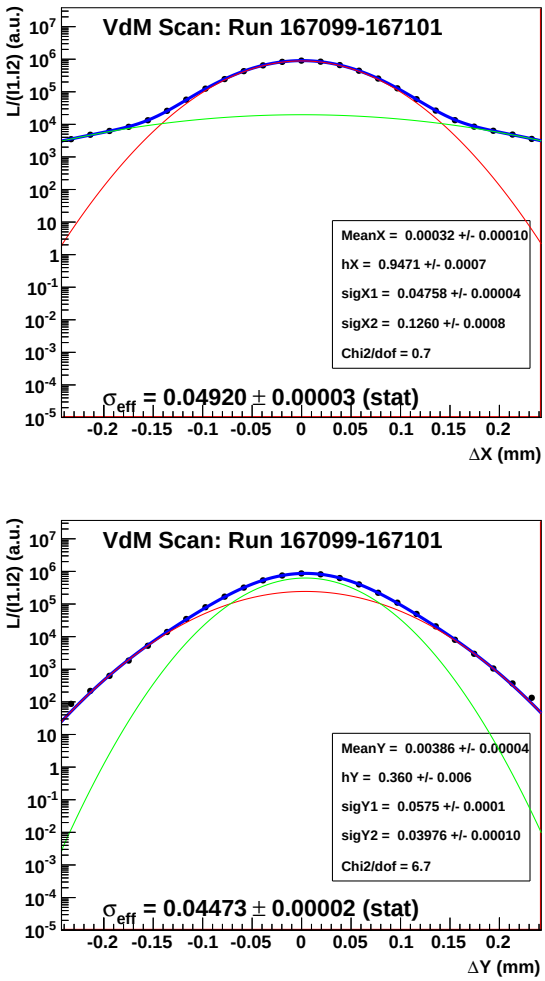

Figure 4.2: Van der Meer seperation scans conducted in June 2011, using the tower occupancy method. The fit parameters and the effective sigma are listed on the plots in mm.

4.2 Non-Linearity of the HF

In 2011, the CMS collaboration found that the relative instantaneous luminosity readings from the HF calorimeters do not have a linear response; at high instantaneous per-bunch luminosities the reading is higher than it should be [10]. This was discovered by looking at the cross-section for finding primary vertices as a function of the instantaneous per-bunch luminosity. The cross-section should ideally be constant, but it was found to decrease as instantaneous per-bunch luminosity increased, indicating two possibilities:

- The efficiency of finding primary vertices decreases as instantaneous per-bunch luminosity increases.
- The relative instantaneous luminosity readings from the HF calorimeters is increasingly overestimated as instantaneous per-bunch luminosity increases.

The first possibility was ruled out by checking the vertex cross-section by another method and both methods came to very nearly the same cross-section. The second possibility was confirmed when a similar effect was seen when looking at the event rate for tracks.

A simple linear correction was devised to correct for the non-linearity of the HF luminosity data:

$$\mathcal{L} = \mathcal{L}_{\mathrm{HF}}(1 - \alpha \frac{d\mathcal{L}}{dt}), \tag{4.2}$$

where $\mathcal{L}$ is the luminosity, $\mathcal{L}_{\mathrm{HF}}$ is the raw luminosity as reported by the HF calorimeters, $d\mathcal{L}/dt$ is the instantaneous per-bunch luminosity in units of Hz/μb and α is our non-linearity correction coefficient. The non-linearity correction coefficient was determined to be $\alpha = 0.0755$ for the tower occupancy method of the HF calorimeters [10].[2]

As this non-linearity correction affects the data that we use to fit in the Van der Meer scans (Figure 4.1 and Figure 4.2), we must correct the data and perform the fits again in order to obtain corrected effective beam widths σ_{eff}. The HF non-linearity corrected effective beam widths are shown in Table 4.2. The June scan was conducted at a peak instantaneous per-bunch luminosity of 2.5× that of the two May scans, so it is expected that the HF non-linearity correction causes a much larger change in the June scan effective beam widths than in the two May scans.

[2]We independently found the $\sum E_T$ correction to be $\alpha = 0.055$, but for the purposes of conciseness and comparison with the official normaliztion we will focus on the tower occupancy method for the remainder of this section.

Scan		Uncorrected (mm)	HF non-linearity corrected (mm)	Change
May Scan 1	$\sigma_{\text{eff-x}}$	0.05796 ± 0.00005	0.05830 ± 0.00005	0.59%
	$\sigma_{\text{eff-y}}$	0.05590 ± 0.00007	0.05635 ± 0.00008	0.81%
May Scan 2	$\sigma_{\text{eff-x}}$	0.05862 ± 0.00006	0.05894 ± 0.00005	0.55%
	$\sigma_{\text{eff-y}}$	0.05629 ± 0.00008	0.05673 ± 0.00010	0.78%
June Scan	$\sigma_{\text{eff-x}}$	0.04920 ± 0.00003	0.05014 ± 0.00004	1.91%
	$\sigma_{\text{eff-y}}$	0.04473 ± 0.00002	0.04568 ± 0.00002	2.12%

Table 4.2: HF non-linearity corrected and uncorrected effective beam widths calculated for the three Van der Meer scans. No length-scale corrections have been applied.

4.3 Normalization Change

Given our calculated effective beam widths from Table 4.2, we are now ready to calculate the absolute luminosity using Equation (3.14). We also apply the length-scale calibration correction from Equation (4.1). A convenient way to refer to the absolute luminosity calibration constant that we calculate using our 2011 Van der Meer separation scans is to compare it to the 2010 luminosity calibration constant. We do this by introducing a ratio: $r \equiv \mathcal{L}_{2011}/\mathcal{L}_{2010}$.

The luminosity readout system on the HF calorimeters has a phenomenon known as afterglow. This is where it continues to read out some luminosity for empty bunches, as it is leftover response from an earlier bunch collision. Although this afterglow is negligible, with many hundreds of bunches colliding, the cumulative effect can become quite significant. The May scans only had 14 bunches colliding so there the afterglow effect is negligible, but for the June scan it was determined that the ratio r_{June} must be adjusted by a factor of 1.021 [10].

In each scan there are multiple times at which the beams are aligned (no beam separation). For each of these points the ratio r can be calculated, as we know the current at that time and the HF luminosity reading. For the May scan, there is also two $\sigma_{\text{eff-x}}$ and two $\sigma_{\text{eff-y}}$, which creates four possible combinations for the ratio r. We calculate all of them and average.

Including all our corrections (HF non-linearity, length-scale and afterglow), we find the two ratios to be:

$$\begin{aligned} r_{\text{May}} &= 1.102, \\ r_{\text{June}} &= 1.101. \end{aligned} \tag{4.3}$$

This apparent agreement is deceptive, because of the non-linearity in the HF. The June scan had a peak instantaneous per-bunch luminosity of 0.86 Hz/μb, where as the May

scans had a peak instantaneous per-bunch luminosity of 0.34 Hz/μb. To fairly compare them, we must extrapolate both ratios to a common shared instantaneous per-bunch luminosity using Equation (4.2). For convenience we choose to extrapolate both to an instantaneous per-bunch luminosity of zero. After doing this we find:

$$\begin{aligned} r_{\text{May}}^{d\mathcal{L}/dt=0} &= 1.130, \\ r_{\text{June}}^{d\mathcal{L}/dt=0} &= 1.172. \end{aligned} \tag{4.4}$$

The difference of 3.7% between the May and June calibrations is within the uncertainty of the HF luminosity system[3].

It is worth nothing that we do not take into account emittance corrections into our calibration correction ratio. As these are typically on the order of 0.5%, we choose not to include them as they do not change the result that significantly. For example, the emittance corrections for the May scans changed the calibration correction ratio by $\approx 0.2\%$ [10]. As we calculated the normalization changes to show that the May and June scans agree to within the uncertainties of the measurement, this small change is not significant enough. Were we to be calculating the actual calibration for 2011, we would need to take into account the emittance corrections.

4.4 Motivation for $Z \to \mu\mu$ Measurement

Performing the Van der Meer scan calibration for the HF luminosity system using scans made in 2011 has demonstrated to us several weaknesses in the official luminosity measurements, which motivate us to do our study on measuring the integrated luminosity using an independent method. Some of the weaknesses we identify are:

- The beam current measurement from the FBCTs has a 3.1% error, which is the dominant error in the HF luminosity measurement [10]. As this measurement is done by the LHC and is outside of CMS' control, we cannot improve the beam current measurement.

- Corrections for the non-linearity in the HF might not be fully accurate, as only a linear correction was applied. The detector response of the HF might be more complex and require a higher-order correction.

- The afterglow correction depends on the occupancy of all the bunches. In practice,

[3]The HF luminosity system has a uncertainity of 4.5%, so the uncertainity on the difference of two luminosity measurements is $\sqrt{2} \times 4.5\% \approx 6.4\%$

it is assumed that all the bunches are filled uniformly, but this is an approximation [11].

- Every correction (afterglow and HF non-linearity) has a systematic uncertainty associated with it, increasing the overall uncertainty of the luminosity measurement significantly.
- Each correction might be correlated; this would introduce yet more uncertainty.
- There are possible long-term HF drifts in the HF calibration, amounting to a not insignificant error [10].

After the 2011 run at the LHC was completed, study of the year's data confirmed that some of the weaknesses we identified are present. The HF drift was much larger than anticipated: in summer it was given a 1.5% systematic uncertainty, but, at the end of the run, a drift of almost 5% was found [12]. This had to be corrected by another correction, which introduces yet another uncertainty. In future years, the drift needs to be monitored and constantly corrected. The HF non-linearity correction was changed from a linear correction to a quadratic one in the December 2011 update of the `lumicalc.py` program [11], indicating that the linear correction used in the May Van deer Meer scans was not overly accurate. Perhaps this quadratic correction is still not sufficient.

Given the complexity and uncertainty surrounding the various corrections (HF non-linearity, HF drift and afterglow) and the large error of the FBCTs, it is extremely imperative that the official HF measurement of total integrated luminosity be verified, especially given that this is used in almost all measurements at CMS. Our measurement using $Z \to \mu\mu$ decays is able to cross-check the official measurement, as it is a completely independent method that does not share any common weaknesses or systematics.

Chapter 5

$Z \to \mu\mu$ Event Selection

We describe the method and selection cuts that we perform for finding and selecting the $Z \to \mu\mu$ decays used for our measurement of integrated luminosity. We next compare our selection on data of $Z \to \mu\mu$ decays to a Monte Carlo simulation to ensure that our selection works well. We also calculate the kinematical acceptance of the selection cuts that we use in the last section.

5.1 Data and Monte Carlo Samples

5.1.1 Dataset and Reconstruction

The raw data that is read-out from the detector for every event is approximately 1 Mb in size, but CMS computers analyze this raw data offline to produce more concise and useful data files. First the data is decoded and detector calibration and corrections are applied. Next the hits (a location of where a particle passed through) in the silicon tracker and the muon system are used to work out the paths the particles took, known as tracks; this is the most time-consuming task. The start positions of all these tracks are then used to calculate vertex positions. Finally the tracks and energy deposits in the calorimeter are all inputted into various algorithms that reconstruct the physics objects, such as muons, electrons, photons and jets. Generally this entire process is called event reconstruction.

Almost all analyses work with either the `RECO` data format or the `AOD` data format as these contain all the information that one would normally need. The main difference between these two is that the `RECO` data format keeps the tracker and muon hits and the `AOD` data format does not. For our analysis we used the `AOD` data format as it is more compact (taking less time to process) and contains all the information we need. Instead of being 1 Mb in size like the raw data, it is only around 50 Kb in size per event.

Our measurement of total integrated luminosity using $Z \to \mu\mu$ decays is performed using data gathered during 2011 at CMS. The data from 2011 corresponds to a total integrated luminosity (as determined by the current luminosity system) of $\int \mathcal{L} dt = 4.6$ fb^{-1}. More specifically, we use the `SingleMu` data from the `Run2011A` and `Run2011B` datasets. The `SingleMu` data contains all events that were recorded because they triggered a single muon trigger.

We also only use data that has been validated as coming from a good run by CMS. This is given to us in a `JSON` file that lists all the "good" run numbers and lumisections within each run.

5.1.2 Monte Carlo Samples

In Section 5.5 we perform a comparison between Monte Carlo simulations of $Z \to \mu\mu$ decays and the actual data. The Monte Carlo sample used is one that was generated centrally by CMS named `DYToMuMu_M-20_CT10_TuneZ2_7TeV-powheg-pythia` from `Summer11` and corresponds to just over 30 million events of Drell-Yan production of Z bosons decaying to two muons. As explained in Section 1.2, the two processes in Figure 1.1 account for the vast majority of Z boson production; both the LO and NLO process are included in our Monte Carlo sample.

The sample was generated using Powheg [13], a NLO QCD generator, interfaced with another program, Pythia [14], which generates the parton showering. The CT10 parton probability distribution functions were used [15].

5.2 Muon Selection Criteria

On the data we require the `HLT_IsoMu24` trigger to be fired. This trigger requires that the muon that triggered it to have $P_T > 24$ GeV/c ($P_T > 16$ GeV/c cut at the L1 trigger) and be isolated. We further require offline that the muons for the Z candidate must:

- Both be reconstructed as global muons (matches tracks in the silicon tracker and the muon system)
- Both have $P_T > 35$ GeV/c
- Both have opposite charge (as the Z is neutral)
- Both be in the pseudo-rapidity range $|\eta| < 2.1$ (there are issues with the trigger in the forward region of $2.1 < |\eta| < 2.4$)

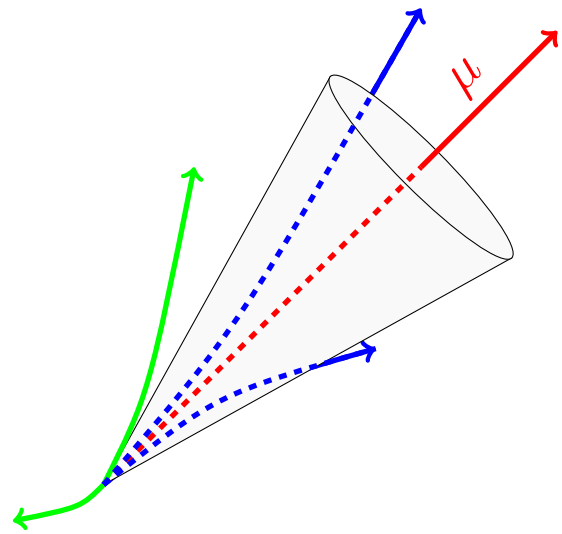

Figure 5.1: The track isolation cone drawn around the red muon: blue tracks are inside the cone and green ones are outside the cone.

- Include at least one muon that caused the `HLT_IsoMu24` trigger to fire (known as matching the trigger)

The muons for the Z candidate must also be isolated. For this analysis we use track isolation as we are not so concerned with calorimeter isolation because we do not use the calorimeters to measure our muons. A cone of aperture $\Delta R \equiv \sqrt{\Delta\eta^2 + \Delta\phi^2} = 0.3$ is drawn around the muon's track in the silicon tracker and the P_T of any tracks that are inside this cone (excluding the muon's track) is summed. We require that

$$\sum_{\text{tracks in cone}} P_T < 3 \text{ GeV/c}. \tag{5.1}$$

Figure 5.1 illustrates this cone isolation process; the P_T of the blue tracks, as they are inside the cone of the red muon, are summed but the green tracks are ignored.

A typical $Z \to \mu\mu$ decay event that is selected by the above criteria is shown in Figure 5.2. There are two muons shown in red and they are both global muons because they have tracks in the silicon tracker and hits in the muon system. It is also worth nothing that the muons have very high P_T (as shown by the low curvature in the tracker) and are well-isolated from other tracks.

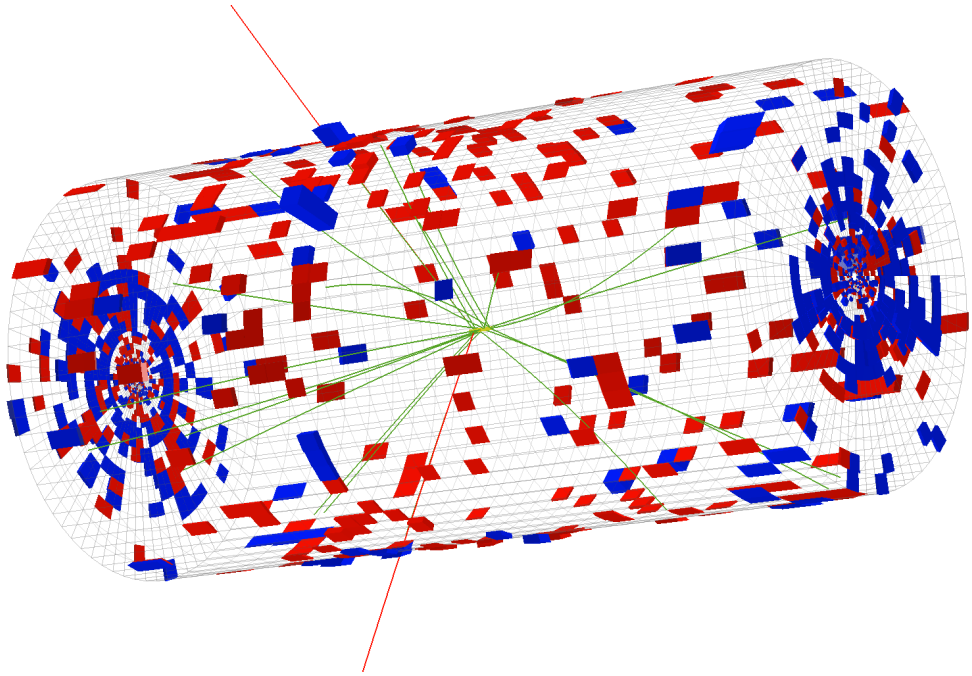

(a) 3D View

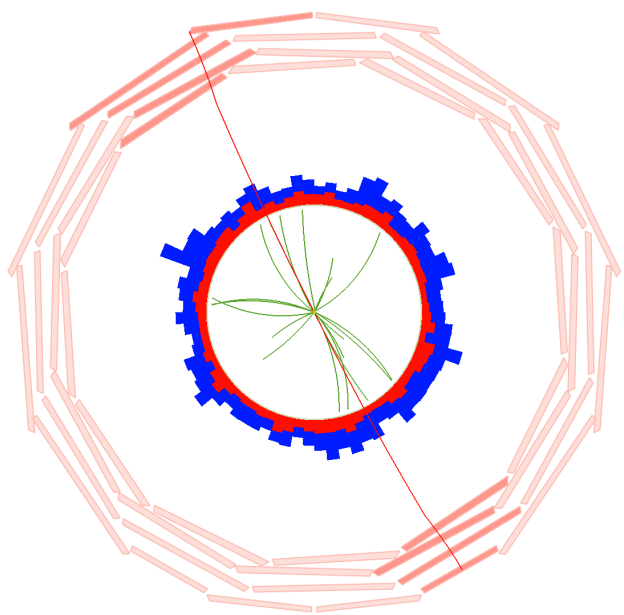

(b) $\rho - \phi$ View

Figure 5.2: The event display for a single $Z \to \mu\mu$ event, made using cmsShow [16]. The event shown is Run 175832, Luminosity Section 108, Event 57849678. The red lines correspond to reconstructed muons and the green lines are reconstructed tracks. The red and blue bars correspond to deposited energy in the electromagnetic and hadron calorimeters respectively. The outer red segments in the ρ–ϕ view are the muon chambers.

5.3 Software Analysis

The main analysis of the data files is done by the `ZMuMu` package [17] within the official CMSSW framework, which we have modified for our own purposes. This is written in a mixture of C++ and Python and run on the CMSLPC supercomputing cluster at Fermilab. The package was first updated to run successfully on the 2011 data and triggers, and next it was modified to use our selection criteria, which differ from the ones previously used by the code. Originally it only recorded the invariant mass of the two muons and their P_T for Z boson candidates, but in order to make the performance plots in Section 5.5 we added additional kinematical variables for it to record.

The main change to this package concerns its output. Previously it created histograms for each of the variables it was recording and stored these in a ROOT file. However, in order to more easily perform some of the analysis in Chapter 8, we changed it to output these variables for every event that passed our selection to a text file, along with the events' run number and lumisection and the instantaneous luminosity of the bunch crossing. This gives us information about every single event instead of the mere overview that the histograms gave us, which, in particular, allows us to do the integrated luminosity measurement on a subset of the data without having to re-run the analysis. As all the information is stored is a strict superset of the original histogram output, we can still create the original histograms if needed.

This output text file was then parsed and analysed using a combination of standard UNIX tools (such as `grep` and `bash`) and the data analysis framework, ROOT [18].

5.4 Background Processes

Although the majority of the background to selecting $Z \to \mu\mu$ decays at the LHC is from QCD multi-jets, there are other background processes that contribute. Here we list the main backgrounds that we expect to appear and how we attempt to reduce their contributions:

- $W^{\pm} \to \mu^{\pm}\nu_{\mu}$: Only one muon is produced via this process, so the other muon we select must come from another process; this reduces this background.
- $t\bar{t}$: Although the top quark can decay leptonically to muons, the production cross-section for $t\bar{t}$ is smaller and so the estimated background is quite small.
- QCD jets: The leptons in these jets are not isolated and our isolation requirement removes much of this background.

- $Z \to \tau^+\tau^-$: Although the two tau leptons can decay into muons, the $P_T > 35$ GeV/c selection cut we have reduces the background from these decays [5].
- WZ, WW and ZZ: These dibosons have a much smaller production cross-section (several orders of magnitude smaller) than the $Z \to \mu\mu$ decays that we wish to select, so the estimated background is very small.

In [19] each background contribution and the signal from Monte Carlo samples was summed, scaling them appropriately to the luminosity of their data sample, and it was found that the number of events selected and the distribution of invariant mass compared well with that from data. This demonstrates that all the backgrounds to our signal were accounted for. The signal to background determined from these Monte Carlo samples was also very high, so the selection we use is good at selecting our signal events.

We estimate the background to be less than 0.1%, by comparing the number of decays in our invariant mass window $M \in (60, 120)$ GeV/c^2 in data to that in the signal Monte Carlo, scaled by the total integrated luminosity of the data. This shown in Figure 5.3.

5.5 Performance Plots

Figure 5.3 through Figure 5.8 show various kinematical distributions (the invariant mass M, transverse momentum P_T, rapidity y and the position in η, ϕ and $\cos\theta$) of the reconstructed Z bosons that we chose from the dataset according to the criteria in Section 5.2. The data is plotted in black with error bars, while the Monte Carlo signal sample is shown by the orange area. The Monte Carlo sample was normalized according to the total integrated luminosity of the data; in other words we scale it by ratio of the integrated luminosity of the data to the integrated luminosity of the sample.

For all these performance plots, there is no cut on the invariant mass of the reconstructed Z boson, but it is worth nothing that our measurement is only done on the mass window of $M \in (60, 120)$ GeV/c^2: when we count the yield of Z bosons we only include those that are in this mass window and we also have a cross-section that takes into account this mass window (see Section 1.3). The invariant mass distribution (Figure 5.3) is also plotted on an extended mass window.

We have chosen not to include any background Monte Carlo sample contributions in our performance plots, as the background is very small compared to the signal. If there were a significant discrepancy between our signal Monte Carlo and the data then this might indicate that there was a sizeable background to our signal. However, we find

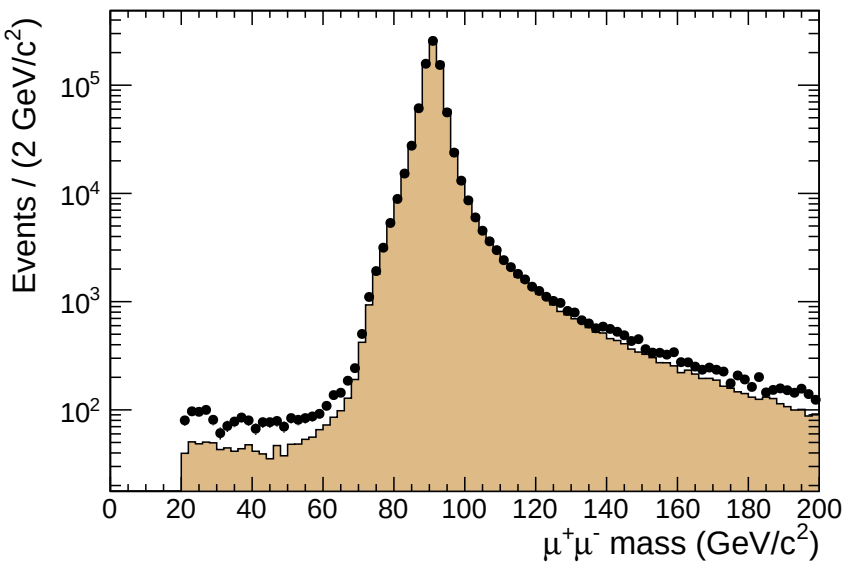

Figure 5.3: The mass distribution of the $Z \to \mu\mu$ decays observed in data and in our Monte Carlo sample.

close agreement between the data and the scaled Monte Carlo signal sample; this shows us that the background to our $Z \to \mu\mu$ selection really is very small. This makes our muonic Z boson decay ideal for making an accurate measurement of total integrated luminosity.

5.6 Kinematic Acceptance

Our $P_T > 35$ GeV/c and $|\eta| < 2.1$ cuts on the muons mean that we are not counting all $Z \to \mu\mu$ decays, as some of these decays will not survive these kinematical cuts. Acceptance corrects for this loss through the A term in Equation (1.3), as it is the fraction of $Z \to \mu\mu$ decays that meet our kinematical selection criteria. As we are performing the entire measurement in the invariant mass window of $M \in (60, 120)$ GeV/c^2 it is equivalent to:

$$A = \frac{N(60 \text{ GeV/c}^2 < M < 120 \text{ GeV/c}^2, P_T > 35 \text{ GeV/c}, |\eta| < 2.1)}{N(60 \text{ GeV/c}^2 < M < 120 \text{ GeV/c}^2)}, \tag{5.2}$$

where N is the number of $Z \to \mu\mu$ decay candidate events found given those selection cuts.

We calculate this by using our code on the generator level of the Monte Carlo sample we have for $Z \to \mu\mu$ decays (see Section 5.1.2 for details on the sample), which consists of

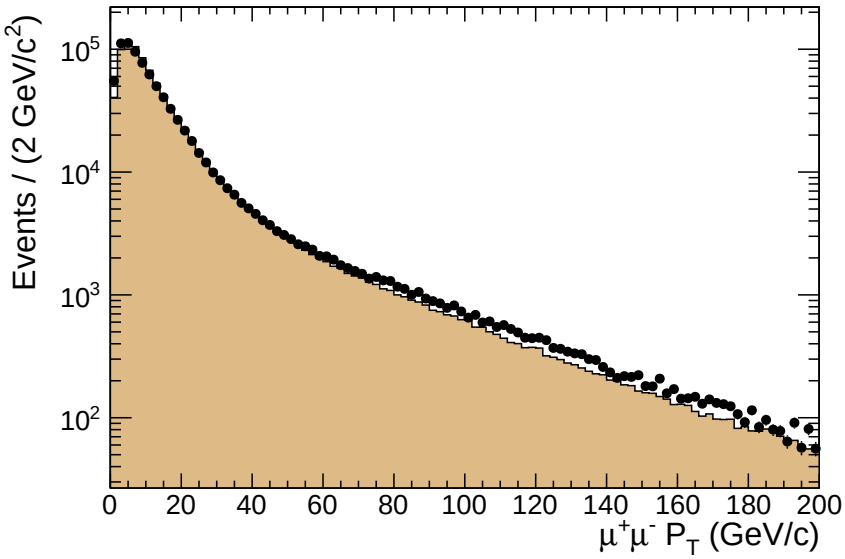

Figure 5.4: The transverse momentum (P_T) distribution of the $Z \to \mu\mu$ decays observed in data and in our Monte Carlo sample.

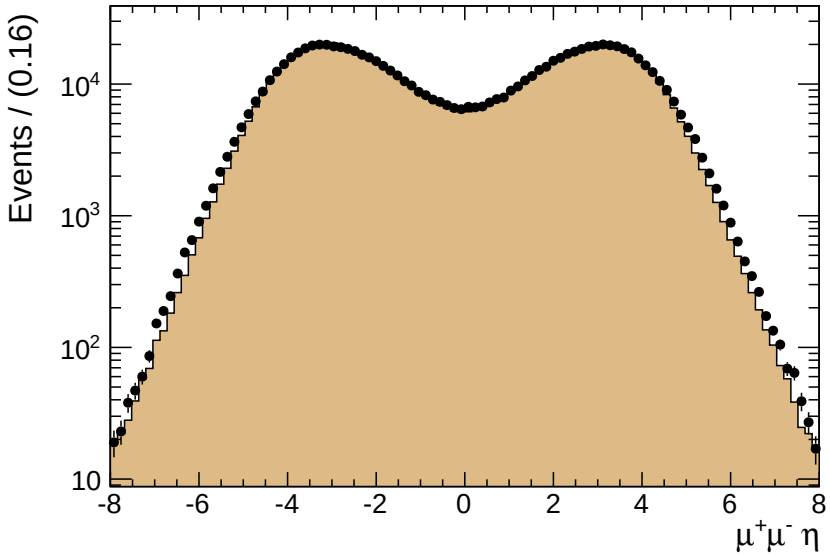

Figure 5.5: The η distribution of the $Z \to \mu\mu$ decays observed in data and in our Monte Carlo sample.

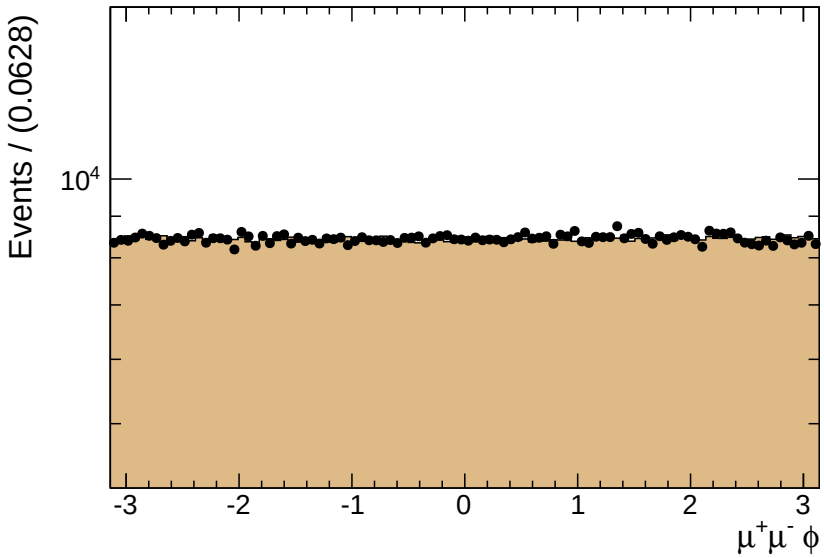

Figure 5.6: The ϕ distribution of the $Z \to \mu\mu$ decays observed in data and in our Monte Carlo sample.

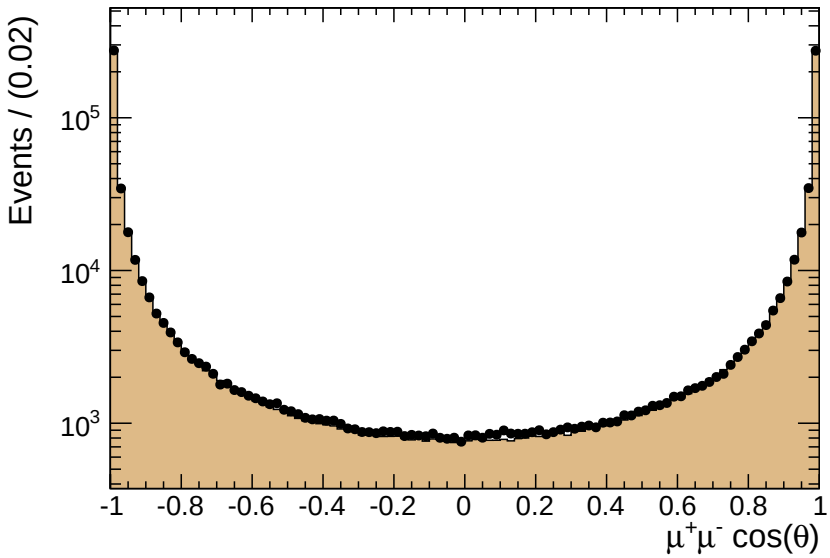

Figure 5.7: The $\cos(\theta)$ distribution of the $Z \to \mu\mu$ decays observed in data and in our Monte Carlo sample.

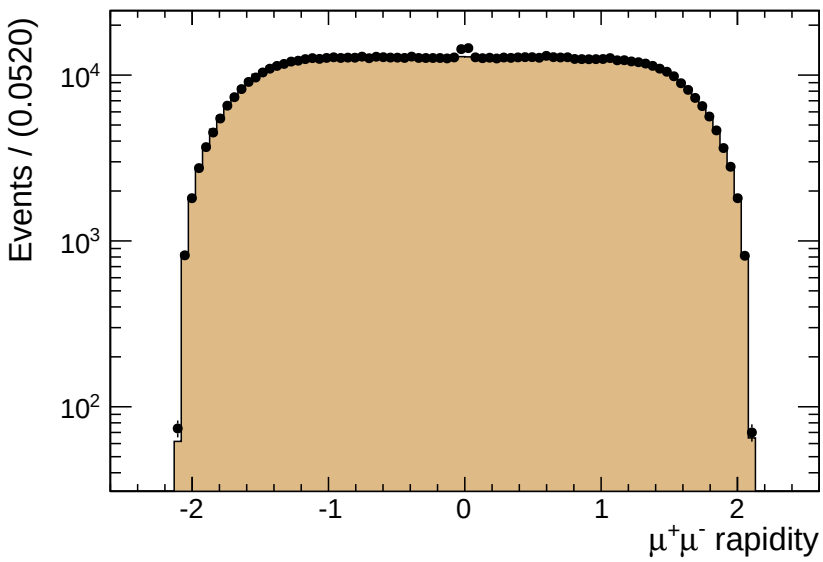

Figure 5.8: The rapidity (y) distribution of the $Z \to \mu\mu$ decays observed in data and in our Monte Carlo sample.

only simulated $Z \to \mu\mu$ decays. In addition to the hits and energy deposits that would be recorded by the detector, the Monte Carlo simulator stores the information and tracks of all particles for each event in the data file. Rather than using the reconstructed particles (reconstructed on the hits and energy deposits), we can use the stored particles; this is known as using the generator level. By using the generator level, our acceptance will not be biased by reconstruction and detector inefficiencies and will solely represent the kinematical acceptance.

We found that the kinematical acceptance for our $P_T > 35$ GeV/c and $|\eta| < 2.1$ cuts on the muons is:

$$A = 0.232. \tag{5.3}$$

The uncertainty on this value is treated separately in Chapter 7.

We can estimate the number of decay events we expect to find for our data by $N = \sigma \times \mathcal{B} \times A \times \epsilon \times \int \mathcal{L} dt$. Although we address the efficiency in the next chapter, for the purposes of this rough estimate we assume the efficiency is very nearly one. For our 2011 data which has an integrated luminosity (as determined by the current luminosity system) of $\int \mathcal{L} dt = 4.6$ fb^{-1}, we can expect to find around a million $Z \to \mu\mu$ decay events. This number is very plentiful and will allow us to achieve high statistical accuracy even on much smaller datasets, enabling us to make our measurement of integrated

luminosity on only a few hours of data.

Chapter 6

Muon Efficiency and Yield

In order to get the efficiency-corrected yield in Equation (1.2), we need to determine the efficiency of our muon selection criteria, listed in Section 5.2. We do this by using the Tag and Probe (TP) method on the muons in our $Z \to \mu\mu$ decays.

This is a data-driven approach that does not rely on any Monte Carlo samples. The advantage of this is that we avoid any possible systematic errors that are introduced by the Monte Carlo simulation. For an accurate determination of the efficiencies and the total yield, this data-driven approach can only be done if we have sufficient data to get good statistics in the five event categories. Fortunately, as described in Section 1.4, we have copious production of Z bosons so this is not a problem.

The overall muon efficiency to can be broken down into several consecutive steps:

1. Acceptance $\to$ Standalone muon[1]: ϵ_{sa}, as it is the efficiency for the muon system to reconstruct standalone muon tracks

2. Standalone muon $\to$ Global muon[2]: ϵ_{trk}, as it is the efficiency for the inner silicon tracker to reconstruct tracks for the muons

3. Global muon $\to$ Isolated Global muon: ϵ_{iso}, as it is the efficiency of isolation

4. Isolated Global muon $\to$ Triggered Isolated Global muon: ϵ_{HLT}, as it is the efficiency for the high level trigger to trigger on the muon

[1]Standalone muons are muons that are only reconstructed in the outer muon system and is not matched to tracks in the inner silcon tracker

[2]Global muons are standalone muons that have been matched to tracks in the inner silicon tracker

6.1 Overview of the Tag and Probe Method

We require one muon to meet our stringent selection criteria; this is known as the tag muon. For the other muon, known as the probe muon, we then see if it can pass a chosen efficiency step. If it can, then we classify the event as a Tag+Pass event. If not, then we classify it as a Tag+Fail event.

We construct two histograms of invariant mass corresponding to each classification and fill them accordingly from our events in data. We then use a fit to determine the yield of signal and background events in each classification. The efficiency for the step we chose is then simply:

$$\epsilon = \frac{N_{\text{pass}}^{\text{signal}}}{N_{\text{pass}}^{\text{signal}} + N_{\text{fail}}^{\text{signal}}}. \tag{6.1}$$

6.2 Simultaneous Fit using Five Event Categories

Typically each efficiency step is extracted individually using a Tag and Probe study for each one as outlined in the previous section. However, we extract the signal yield and muon efficiencies from a single simultaneous fit on the distribution of invariant mass, as this accounts for any correlations between the efficiency-corrected yield and the muon efficiencies, resulting in a smaller uncertainty on the efficiency-corrected yield.

We define the following five event categories that we sort the Z decays into, following the treatment in [19]:

- $Z_{\mu\mu}^{\text{2HLT}}$: two isolated global muons, each matching the trigger.
- $Z_{\mu\mu}^{\text{1HLT}}$: two isolated global muons, with only one matching the trigger.
- $Z_{\mu s}$: one isolated global muon matched to the trigger and one isolated standalone muon.
- $Z_{\mu t}$: one isolated global muon matched to the trigger and one isolated track.
- $Z_{\mu\mu}^{\text{noniso}}$: two global muons, at least one of which is non-isolated and at least one of which is matched to the trigger.

While the tag muon selection criteria remain the same, each category varies the selection criteria on the probe muon, so that with these five categories we can extract the efficiencies of all four reconstruction steps as well as the total signal efficiency-corrected yield. These categories are mutually exclusive in order to prevent multiple counting of decays. When evaluating which category to assign a certain event to, the categories are

assessed in the above order and the first one that matches is chosen. The number of events recorded in each category for the 2011 data is listed in Table 6.1.

Category	Number of Events	Percentage
$Z_{\mu\mu}^{\mathrm{2HLT}}$	661,330	67.0 %
$Z_{\mu\mu}^{\mathrm{1HLT}}$	247,879	25.1 %
$Z_{\mu s}$	8,951	0.9 %
$Z_{\mu t}$	38,291	3.9 %
$Z_{\mu\mu}^{\mathrm{noniso}}$	29,952	3.0 %
Total	986,373	–

Table 6.1: The number of events recorded in each event category for the 2011 data, corresponding to 4.6 fb^{-1}.

Next we calculate each category's total efficiency term, which is the product of individual efficiency terms corresponding to selection criteria:

- $Z_{\mu\mu}^{\mathrm{2HLT}}$: both muons must be isolated ($\epsilon_{\mathrm{iso}}^2$), both muons must be reconstructed in the muon system (ϵ_{sa}^2) and have tracks in the inner silicon tracker ($\epsilon_{\mathrm{trk}}^2$) and the HLT trigger must fire on both ($\epsilon_{\mathrm{HLT}}^2$).

- $Z_{\mu\mu}^{\mathrm{1HLT}}$: the isolation, the track and muon system reconstruction is the same as $Z_{\mu\mu}^{\mathrm{2HLT}}$, but the HLT trigger must fire on one and not the other ($2\epsilon_{\mathrm{HLT}}(1-\epsilon_{\mathrm{HLT}})$).[3]

- $Z_{\mu s}$: the isolation and muon system efficiency terms are the same as $Z_{\mu\mu}^{\mathrm{2HLT}}$, but only one of the muons is found in the inner silicon tracker ($2\epsilon_{\mathrm{trk}}(1-\epsilon_{\mathrm{trk}})$) and the HLT trigger now has to trigger on the only global muon (ϵ_{HLT}).

- $Z_{\mu t}$: this is the same as the $Z_{\mu s}$ category, but with the standalone and track terms swapped.

- $Z_{\mu\mu}^{\mathrm{noniso}}$: both muons are global so the track and muon system reconstruction is the same as $Z_{\mu\mu}^{\mathrm{2HLT}}$, but at least one of the muons must be non-isolated ($1-\epsilon_{\mathrm{iso}}^2$),[4] and at least one of the muons must be matched to the trigger, which is $1-(1-\epsilon_{\mathrm{HLT}})^2$.[5]

[3] The factor of two is due to the combinatorics of choosing one muon from two, i.e. the binomial coeffecient for $\binom{2}{1}$

[4] This is one minus both being isolated

[5] This is one minus both not matching the trigger.

To summarize the above, the total efficiency terms for the five categories are:

$$\begin{aligned}
\epsilon_{\mu\mu}^{\text{2HLT}} &= \epsilon_{\text{HLT}}^2 \epsilon_{\text{iso}}^2 \epsilon_{\text{trk}}^2 \epsilon_{\text{sa}}^2, \\
\epsilon_{\mu\mu}^{\text{1HLT}} &= 2\epsilon_{\text{HLT}}(1-\epsilon_{\text{HLT}})\epsilon_{\text{iso}}^2 \epsilon_{\text{trk}}^2 \epsilon_{\text{sa}}^2, \\
\epsilon_{\mu s} &= 2\epsilon_{\text{HLT}} \epsilon_{\text{iso}}^2 \epsilon_{\text{trk}}(1-\epsilon_{\text{trk}})\epsilon_{\text{sa}}^2, \\
\epsilon_{\mu s} &= 2\epsilon_{\text{HLT}} \epsilon_{\text{iso}}^2 \epsilon_{\text{trk}}^2 \epsilon_{\text{sa}}(1-\epsilon_{\text{sa}}), \\
\epsilon_{\mu\mu}^{\text{noniso}} &= (1-(1-\epsilon_{\text{HLT}})^2)(1-\epsilon_{\text{iso}}^2)\epsilon_{\text{trk}}^2 \epsilon_{\text{sa}}^2.
\end{aligned} \tag{6.2}$$

6.3 Probabilty Density Functions for Signal and Background

The density functions, $f(m)$, that we attempt to fit to the data for each category have a signal component, using the normalized probability density function $s(m)$ for the signal's shape, and a background component, using the normalized probability density function $b(m)$ for the background's shape. The signal's probability density function is multiplied by the total efficiency term for that category and the total number of actual $Z \to \mu\mu$ decays, $\mathcal{N}$. The background's probability density function is multiplied by the total number of background events in the category, N^b.

These density functions are:

$$\begin{aligned}
f_{\mu\mu}^{\text{2HLT}}(m) &= \mathcal{N}\epsilon_{\mu\mu}^{\text{2HLT}} s_{\mu\mu}(m), \\
f_{\mu\mu}^{\text{1HLT}}(m) &= \mathcal{N}\epsilon_{\mu\mu}^{\text{1HLT}} s_{\mu\mu}(m), \\
f_{\mu s}(m) &= \mathcal{N}\epsilon_{\mu s} s_{\mu s}(m) + N_{\mu s}^b b_{\mu s}(m), \\
f_{\mu t}(m) &= \mathcal{N}\epsilon_{\mu t} s_{\mu\mu}(m) + N_{\mu t}^b b_{\mu t}(m), \\
f_{\mu\mu}^{\text{noniso}}(m) &= \mathcal{N}\epsilon_{\mu\mu}^{\text{noniso}} s_{\mu\mu}(m) + N_{\mu\mu}^{b\ \text{noniso}} b_{\mu\mu}^{\text{noniso}}(m).
\end{aligned} \tag{6.3}$$

It is worth noting here that neither the $Z_{\mu\mu}^{\text{2HLT}}$ nor the $Z_{\mu\mu}^{\text{1HLT}}$ categories have a background term. This is because these two categories are almost entirely signal and have a very low background (see Section 5.4).

To construct our signal probability density function, $s(m)$, we use both the $Z_{\mu\mu}^{\text{2HLT}}$ category and the $Z_{\mu\mu}^{\text{1HLT}}$, because these two categories have virtually no background contamination. In order to get more events used in our PDF construction and therefore a more accurate and smooth PDF, we define an additional category $Z_{\mu\mu}$ that is the union of $Z_{\mu\mu}^{\text{2HLT}}$ and $Z_{\mu\mu}^{\text{1HLT}}$ and use this for our PDF construction [19]. This category was the one used for the performance plots in Section 5.5, with the two isolated global muon requirement and the at least one trigger match requirement, detailed in Section 5.2.

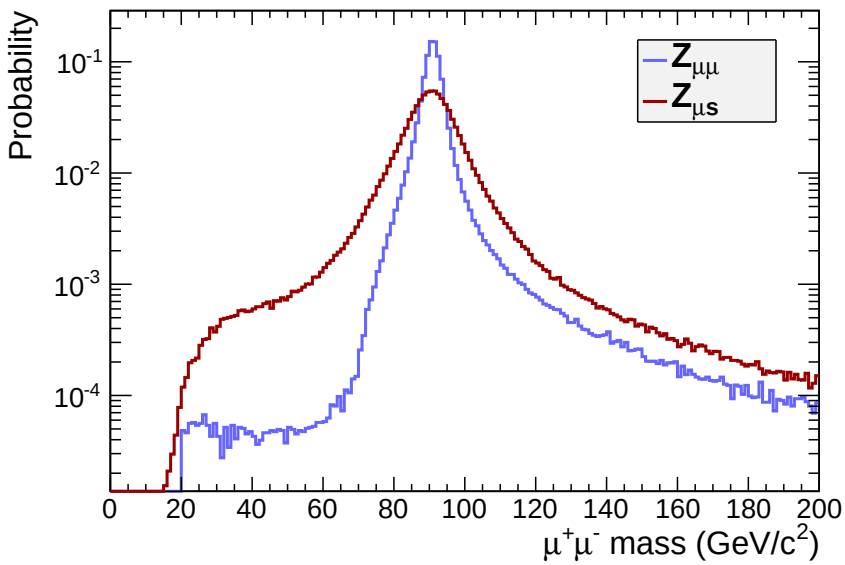

Figure 6.1: The two signal probablity density functions used for fitting the event categories.

For all the categories involving two tracks in the inner silicon tracker (i.e. $Z_{\mu\mu}^{\mathrm{2HLT}}$, $Z_{\mu\mu}^{\mathrm{1HLT}}$, $Z_{\mu t}$ and $Z_{\mu\mu}^{\mathrm{noniso}}$), we use a common signal probability density function, $s_{\mu\mu}(m)$. This is because all four categories use the track fits to determine the momentum and therefore the mass measurements will have the same resolution. We simply take the mass distribution of $Z_{\mu\mu}$ that has virtually no background, making sure to normalize it such that the integral of all its bins is unity.

The $Z_{\mu s}$ category uses a different signal probability density function, $s_{\mu s}(m)$, because one of the muon's momentum is not determined using its track and is instead determined using the outer muon system, leading to a different measurement resolution. To simulate a background-free $Z_{\mu s}$ mass distribution, we use the nearly background-free events in the $Z_{\mu\mu}$ category, but we use the momentum measured from the outer muon system's track fits for one of the muons instead of the inner silicon tracker's track fits when doing the invariant mass calculation [19]. This mass distribution is then normalized to unity.

The signal shape for all categories is entirely data-driven. Figure 6.1 shows both the signal probability density functions, $s_{\mu\mu}(m)$ and $s_{\mu s}(m)$, that we use in the fits, plotted on the same graph for comparison purposes.

For the background probability density functions, $b(m)$, we use a second-order polynomial multiplied by a exponential decay. This is a standard function form that is used for fitting backgrounds. For each category (excluding $Z_{\mu\mu}^{\mathrm{2HLT}}$ and $Z_{\mu\mu}^{\mathrm{1HLT}}$, as these have

no background component), these are:

$$\begin{aligned} b_{\mu s}(m) &= (1 + \alpha_{\mu s} m + \beta_{\mu s} m^2) e^{-\lambda_{\mu s} m}, \\ b_{\mu t}(m) &= (1 + \alpha_{\mu t} m + \beta_{\mu t} m^2) e^{-\lambda_{\mu t} m}, \\ b_{\mu\mu}^{\text{noniso}}(m) &= (1 + \alpha_{\mu\mu}^{\text{noniso}} m + \beta_{\mu\mu}^{\text{noniso}} m^2) e^{-\lambda_{\mu\mu}^{\text{noniso}} m}. \end{aligned} \tag{6.4}$$

Putting all these equations together, we have a total of 17 different variables that we can modify in order to optimize the fit. These are listed in Table 6.2.

6.4 χ^2 Goodness of Fit

We use the well-known χ^2 metric to determine the goodness of the fit. This is defined as:

$$\begin{aligned} \chi^2 &\equiv \sum_i \frac{(O_i - E_i)^2}{\sigma_i^2} \\ &= \sum_i \frac{(O_i - E_i)^2}{O_i}, \end{aligned} \tag{6.5}$$

where O_i is the observed number of events for the ith bin, σ_i is the uncertainty in the observed number of events for the ith bin and E_i is the expected number of events for the ith bin as determined by our equations. The uncertainty in a counting measurement is the square root of the number ($\sigma_i = \sqrt{O_i}$), hence the simplification.

A smaller χ^2 indicates a better fit. Our fitter, therefore, seeks to minimize, R:

$$R = \frac{(N_{\mu\mu}^{\text{2HLT}} - \mathcal{N}\epsilon_{\mu\mu}^{\text{2HLT}})^2}{N_{\mu\mu}^{\text{2HLT}}} + \frac{(N_{\mu\mu}^{\text{1HLT}} - \mathcal{N}\epsilon_{\mu\mu}^{\text{1HLT}})^2}{N_{\mu\mu}^{\text{1HLT}}} + (\chi^2)_{\mu s} + (\chi^2)_{\mu t} + (\chi^2)_{\mu\mu}^{\text{noniso}}. \tag{6.6}$$

The first two terms corresponding to $Z_{\mu\mu}^{\text{2HLT}}$ and $Z_{\mu\mu}^{\text{1HLT}}$ are still using a χ^2 fit, but, because we are using them for the shape of the signal, $s_{\mu\mu}(m)$, we do not sum over every bin but only use the total number of events in calculating χ^2.

6.5 Results

We perform the fit in our invariant mass window ($M \in (60, 120)$ GeV/c^2). As our histograms are created with bins of size 2 GeV/c^2, we have $1 + 1 + 3 \times 30 = 92$ terms in R. Our fit therefore has $92 - 17 = 75$ degrees of freedom.

Table 6.2 contains the results of doing the simultaneous χ^2 fit on our data, which corresponds to 4.6 fb^{-1} of integrated luminosity. In the table, we list both the initial

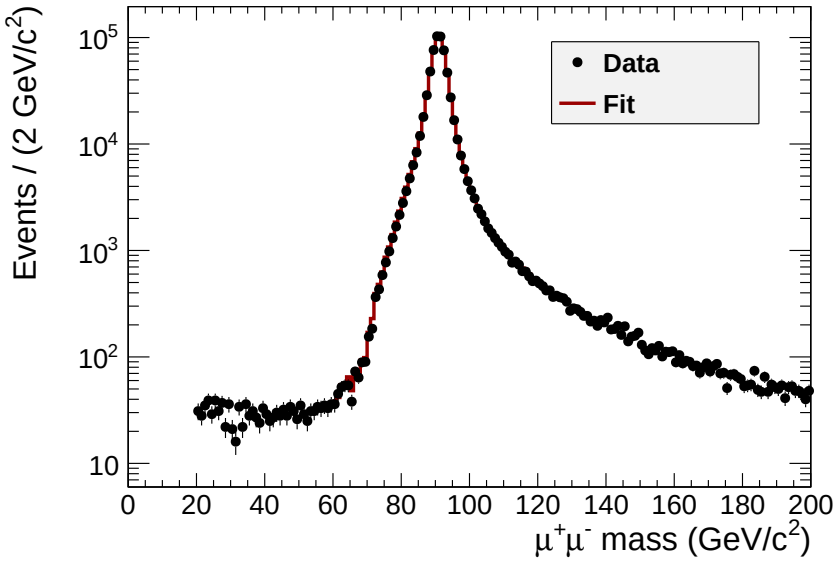

Figure 6.2: The fit superimposed on the invariant mass distribution of $Z \to \mu\mu$ decays in the $Z_{\mu\mu}^{\text{2HLT}}$ category.

guess that we give the fitter as well as the final fitted value. The final χ^2/ndof for the fit divided by the number of degrees of freedom (ndof) is also provided. Although the χ^2/ndof is a little higher than one, the fact that it is close to one shows that the fitter has managed to minimize χ^2 reasonably well and that the fit is decent. Figure 6.2 through Figure 6.6 show the fitted function overplotted on the data, with the fitted background component in green. The fits appear to match the data extremely well in our fit region of $M \in (60, 120)$ GeV/c^2. Both the χ^2/ndof and the good visual fit in our plots indicate that the efficiencies ϵ and total yield $\mathcal{N}$ obtained through our simultaneous fit are very accurate.

The isolation, track reconstruction and muon system efficiencies are all very good as they are ≈ 0.98 and higher. The HLT muon trigger is by far the most inefficient component of the detector where it misses approximately 15% of the high P_T muons. When the luminosity increases at the LHC, the single muon triggers that we use may have to be removed from the trigger menu, as it will take a lot of the trigger bandwidth (the data rate that we can save is limited). Double muon triggers would use less trigger bandwidth and could be used for this measurement. Although this would increase the inefficiency of triggering and reduce the number of events we have to analyse, the loss would not be too great as shown by our HLT efficiency term, ϵ_{HLT}.

Variable	Initial Value	Fitted Value
$\mathcal{N}$	$1,000,000$	$982,512 \pm 1,034$
ϵ_{HLT}	0.85	0.8439 ± 0.0003
ϵ_{iso}	0.98	0.9804 ± 0.0001
ϵ_{trk}	0.99	0.99806 ± 0.00005
ϵ_{sa}	0.98	0.9820 ± 0.0001
$N^b_{\mu s}$	10	0.637 ± 0.300
$N^b_{\mu t}$	10	3.56 ± 1.00
$N^{b\ \mathrm{noniso}}_{\mu\mu}$	10	5.48 ± 1.82
$\alpha_{\mu s}$	-3	-0.572 ± 0.396
$\beta_{\mu s}$	0.025	0.0241 ± 0.0081
$\lambda_{\mu s}$	-0.05	-0.0327 ± 0.0022
$\alpha_{\mu t}$	3	-4.08 ± 0.47
$\beta_{\mu t}$	0.025	0.0809 ± 0.0085
$\lambda_{\mu t}$	-0.05	-0.0378 ± 0.0029
$\alpha^{\mathrm{noniso}}_{\mu\mu}$	3	-3.40 ± 0.33
$\beta^{\mathrm{noniso}}_{\mu\mu}$	-0.05	0.0588 ± 0.0056
$\lambda^{\mathrm{noniso}}_{\mu\mu}$	-0.05	-0.0139 ± 0.0030
χ^2/ndof		1.56

Table 6.2: The seventeen variables that are used in the simultaneous χ^2 fit of invariant mass distribution of the five event categories. Both the initial and fitted values (with statistical uncertainity) are listed.

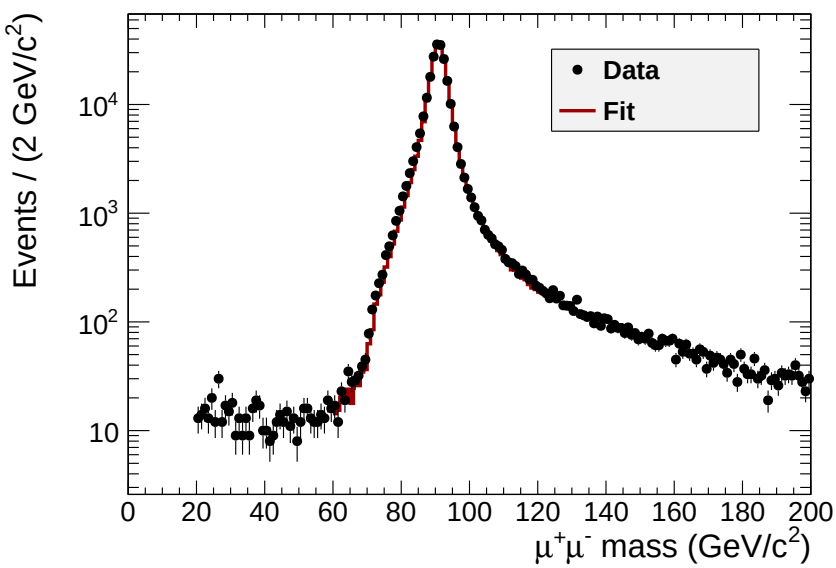

Figure 6.3: The fit superimposed on the invariant mass distribution of $Z \to \mu\mu$ decays in the $Z^{1\mathrm{HLT}}_{\mu\mu}$ category.

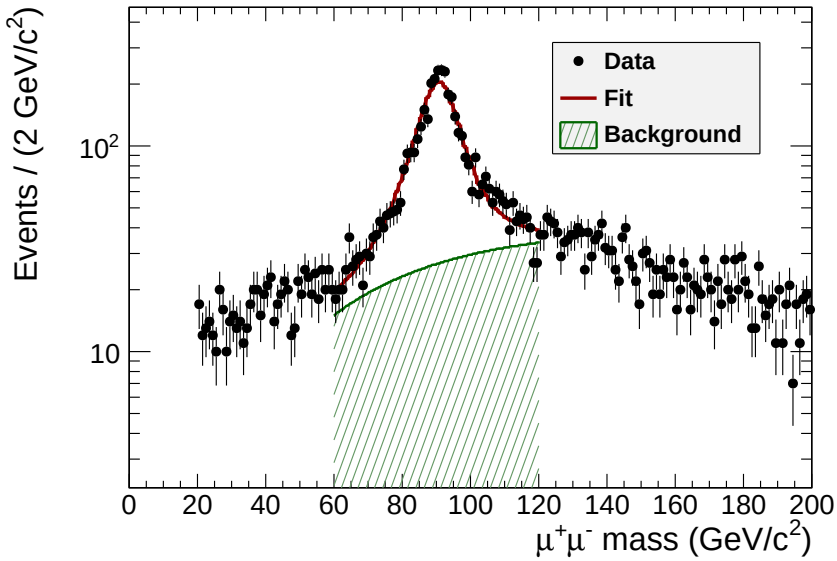

Figure 6.4: The fit superimposed on the invariant mass distribution of $Z \to \mu\mu$ decays in the $Z_{\mu s}$ category.

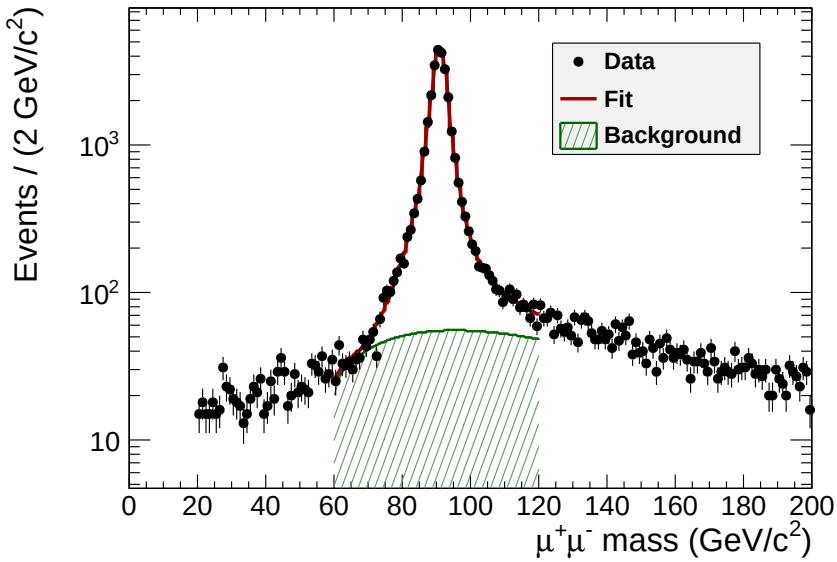

Figure 6.5: The fit superimposed on the invariant mass distribution of $Z \to \mu\mu$ decays in the $Z_{\mu t}$ category.

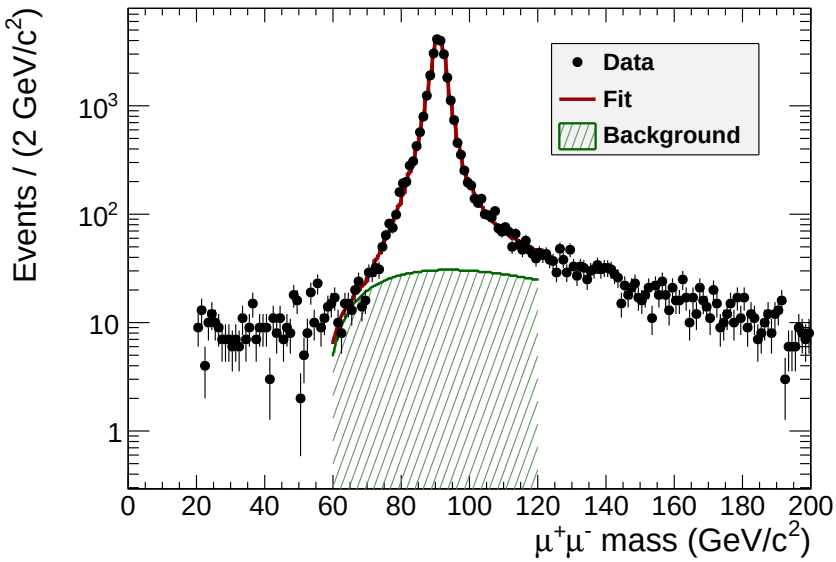

Figure 6.6: The fit superimposed on the invariant mass distribution of $Z \to \mu\mu$ decays in the $Z_{\mu\mu}^{\text{noniso}}$ category.

Chapter 7

Uncertainties in the Measurement

Recall from Equation (1.3) that our total integrated luminosity measurement relies on three quantities: the theoretical cross-section and branching ratio $\sigma \times B$, the efficiency-corrected yield N/ϵ and the acceptance A. In this chapter we examine the uncertainties for each of these three quantities and calculate a total uncertainty on our integrated luminosity measurement.

7.1 Statistical Uncertainties

Whenever we have a measurement for the number of events in a event category or a bin of a histogram, the uncertainty for this measurement due to statistical fluctuations is simply $\sqrt{N}$, where N is the number measured. During our simultaneous χ^2 fit for the efficiency-corrected yield (detailed in Section 6.3), we take this uncertainty in our number of events into account through Equation (6.5), the equation for the reduced χ^2. The fitting program also uses the uncertainty on each measurement to calculate an uncertainty on each fitted variable, listed in Table 6.2. For our calculation on the 2011 data, the statistical uncertainty is 0.105%.

7.2 Systematic Uncertainties

We assumed during our simultaneous χ^2 fit that the $Z_{\mu\mu}^{\mathrm{2HLT}}$ and $Z_{\mu\mu}^{\mathrm{1HLT}}$ categories had no background. However, this is not quite true; there is a background that amounts to no more than 0.5%. This error was estimated by the CMS collaboration by adding a flat distribution to the signal shapes for those two categories and seeing how much the

fitted yield $\mathcal{N}$ changed. [5] found that yield changed by approximately one-third of the background fraction, so with less than 0.5% background fraction (see Section 5.4) we can use 0.2% as a conservative estimate of the systematic error due to the background in the $Z_{\mu\mu}^{\mathrm{2HLT}}$ and $Z_{\mu\mu}^{\mathrm{1HLT}}$ categories. Although the signal probability density functions in the simultaneous χ^2 fit were data-driven, the background probability density functions were not. Different background functions were tried by the CMS collaboration in order to estimate the uncertainty, and half of the difference between the largest and smallest fitted yields was taken as a systematic error. [5] found the uncertainty to be 0.2%. In order to get the total systematic uncertainty for the efficiency-corrected yield N/ϵ, we add the two components in quadrature and obtain 0.3%.

Although the Monte Carlo sample that we use to evaluate the acceptance in Section 5.6 has pileup simulated, the distribution for the pileup (measured by the number of primary vertices) in the Monte Carlo sample does not match that seen in data. To make it more accurate, we reweight the Monte Carlo sample to make the two distributions match. A very conservative estimate of the uncertainty caused by this pileup reweighting is to compare the acceptance calculated by the reweighted Monte Carlo and that calculated by the non-reweighted Monte Carlo; this yields an uncertainty of 0.5%.

There is also a systematic uncertainty associated with the resolution of the detector in measuring momentum (and therefore invariant mass). This has been estimated at less than 0.1% for 2011 and therefore we can ignore it as it is negligible.

7.3 Theoretical Uncertainties

The acceptance value, shown in Equation (5.3), is also subject to a large number of uncertainties that derive from various theoretical assumptions. The Monte Carlo generator we use to evaluate acceptance (Powheg) only performs calculations at next-to-leading order (NLO), so it neglects to take into account higher-order effects, initial-state and final-state radiation, electroweak corrections and a few other phenomena. The acceptance value calculated also depends on the parton distribution function (PDF) sets used, so if we look at the variation caused by using other PDF sets we can estimate a systematic uncertainty. [5] found the acceptance value to have a theoretical uncertainty of 1.9%.

The theoretical cross-section was calculated at next-to-next-to-leading order (NNLO); this means that QCD calculations should be very precise. However, the theoretical cross-section has some uncertainties surrounding the strong coupling α_S and mass of the charm and bottom quark [5]. There are also higher-order corrections beyond NNLO that the program used to calculate the theoretical cross-section (FEWZ) does not take

Source of Error	Fractional Error (%)
Yield (statistical)	0.1
Yield (background subtraction)	0.3
Pileup reweighting	0.5
Acceptance	1.9
Theoretical cross-section	2.7
Total	3.4

Table 7.1: The uncertainities in our measurement of integrated luminosity.

into account. The error on the theoretical cross-section $\sigma \times B$ was listed in Equation (1.4) as 2.7%.

7.4 Total Uncertainty

All the various errors have been listed in Table 7.1. As all the errors are independent and uncorrelated, we can just add their effects in quadrature, leading to a total uncertainty on our total integrated luminosity measurement of 3.4%.

Technically, as both the acceptance and the theoretical cross-section share a systematic uncertainty due to the parton distribution functions (PDF) we cannot add them in quadrature. In theory we also have to add on a term including the correlation between the acceptance and the cross-section. However, determining the correlation is less than trivial and beyond the scope of this paper, so we will just assume that they are uncorrelated.

Chapter 8

$Z \to \mu\mu$ Integrated Luminosity Measurements

In the previous two chapters, we have shown how we get the efficiency-corrected yield through the simultaneous χ^2 fit and the acceptance. Once it is combined with the theoretical cross-section, we now have all the tools necessary to make the total integrated luminosity measurement. In this chapter, we present our measurement using $Z \to \mu\mu$ decays on the total dataset for 2011 and compare it to the official measurement using the Van der Meer scan calibrated HF system. We also probe the stability and consistency of our measurement on many equal-sized segments of the total data.

8.1 Trigger Prescaling

The triggers that we use are sometimes prescaled during the run. Prescaling means that not every event that causes the HLT trigger to fire is recorded, and only every nth event is recorded for a prescaling of n. This, of course, affects our measurement of total integrated luminosity as we have to multiply the factor of n into our luminosity equation, Equation (1.3), in order to get the correct measurement.

When and how much prescaling on our trigger is stored in a central CMS database and can be retrieved. For any given measurement, we simply retrieve the prescaling values, average them over the duration of the data we are looking at and multiply our calculated total integrated luminosity by this value.

8.2 Comparison to Van der Meer Scan Calibrated Luminosity

The total integrated luminosity, determined by the HF luminosity system and calibrated by Van der Meer scans (see Chapter 3), for the dataset we use is:

$$\left(\int \mathcal{L}dt\right)_{\text{VdM}} = 4638 \pm 209 \text{ (syst) pb}^{-1}. \tag{8.1}$$

This was calculated using the official CMS Luminosity Calculation program (`lumiCalc.py`), using version `V03-03-12` [20] and by giving it our list of 'good' lumisections that we use.

From our simultaneous χ^2 fit, the results of which are in Table 6.2, we calculated the total number of $Z \to \mu\mu$ decays in our invariant mass window ($M \in (60, 120)$ GeV/c^2) and our kinematic selection ($P_T > 35$ GeV/c, $|\eta| < 2.1$), $\mathcal{N}$. As this includes the efficiency corrections we can write $\mathcal{N} = N/\epsilon$. The kinematical acceptance, A, that we calculated is in Equation (5.3) and the theoretical cross-section value, $\sigma \times \mathcal{B}$ is in Equation (1.4). Substituting all these into Equation (1.3) we find:

$$\left(\int \mathcal{L}dt\right)_{Z\to\mu\mu} = 4718 \pm 6 \text{ (stat)} \pm 28 \text{ (syst)} \pm 156 \text{ (thry) pb}^{-1}. \tag{8.2}$$

These two calculations of the total integrated luminosity agree with each other to within the uncertainties of the measurements. They only differ by $\approx 0.3\sigma$, which is well below the 1.65σ corresponding to the 95% confidence interval. A visual representation of the two values and their uncertainties is given in Figure 8.1: the blue region is the 1σ confidence interval of the Van der Meer scan-calibrated integrated luminosity and the point and its error bars are the 1σ confidence interval of the $Z \to \mu\mu$ derived integrated luminosity. The overlap in these two measurements show that they agree.

8.3 Stability over Time

For $Z \to \mu\mu$ decays to be used on a regular basis as a measurement of total integrated luminosity, we need to show that the measurement method is stable and consistently works well. To verify its stability, we select the first 4500 pb^{-1} of integrated luminosity from the data, as measured by the official Van der Meer scan calibrated HF system, and split this up into 30 segments of 150 pb^{-1}, performing the $Z \to \mu\mu$ integrated luminosity measurement for each segment.

Rather than running our analysis code 30 times with different ranges of the data to

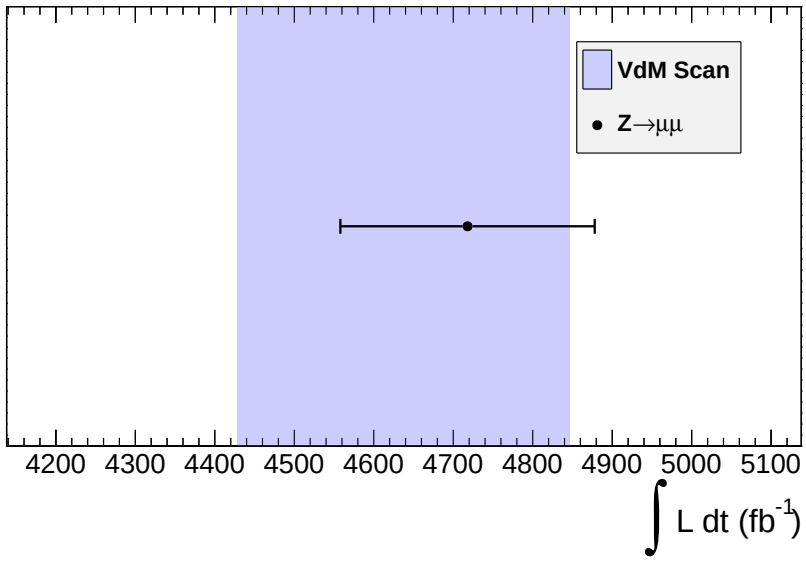

Figure 8.1: A diagram showing calculations of the total integrated luminosity for the 2011 dataset, both from the $Z \to \mu\mu$ method and from the Van der Meer scan calibrated HF system. The confidence intervals shown correspond to 1σ.

analyze, we modified the code so that we could do this time-ordered analysis with only a single run, as explained in Section 5.3. We have a text file that contains the run number and lumisection boundaries that correspond to these 30 segments and we use this to sort the output of our program into the segments (the output has the run number and lumisection and mass of each event) and create an invariant mass distribution histogram for each segment. We then run the fitter on each segment, but because each segment contains vastly less $Z \to \mu\mu$ decays we use different initial guesses for the background yield, N^b, and the signal yield, $\mathcal{N}$. These updated initial guesses are listed in Table 8.1 and the remaining initial parameters are listed in Table 6.2.

Variable	Initial Value
$\mathcal{N}$	30,000
$N^b_{\mu s}$	1
$N^b_{\mu t}$	1
$N^{b\ \text{noniso}}_{\mu\mu}$	1

Table 8.1: The initial guesses for the yield of signal and background used in the simultaneous χ^2 fit for the time-ordered and instantaneous-luminosity-ordered 30 segments of 150 pb^{-1}, as measured by the official Van der Meer scan calibrated HF system.

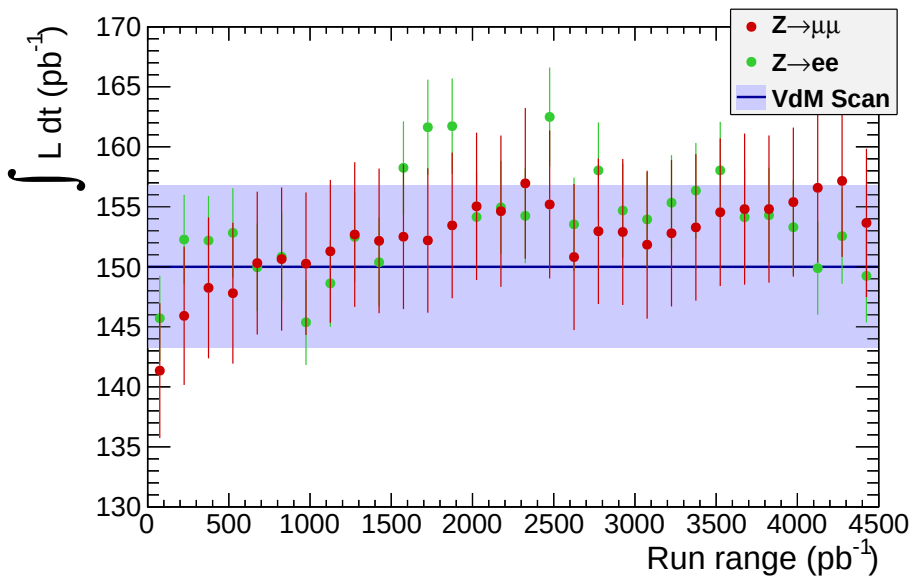

Figure 8.2: Total integrated luminosity for each segment of time-ordered 150 pb^{-1}, as measured by the official Van der Meer scan calibrated HF system. Both the $Z \to \mu\mu$ measurement, the $Z \to ee$ measurement and the Van der Meer scan calibrated measurement are shown with their 1σ uncertainties.

The results of performing the integrated luminosity measurement on each segment is shown in Figure 8.2. The line and the blue region represents the integrated luminosity as reported by the official Van der Meer scan calibrated HF system, including its uncertainty. The red points represent the integrated luminosity according to our $Z \to \mu\mu$ measurement. The uncertainty range and error bars correspond to 1σ. Throughout the run range, the $Z \to \mu\mu$ measurement agrees with the Van der Meer scan calibrated HF system to within their respective uncertainties (represented by the blue region and the red error bars). The $Z \to \mu\mu$ points are also not varying much with respect to time; this shows that using $Z \to \mu\mu$ decays to measure integrated luminosity is stable and consistent.

To check the validity of our fits for each segment, we look at the χ^2/ndof for each fit. These are shown in Figure 8.3, where the red region represents the 5% significance level of the fit. A fit at the 5% significance level means that, if the data were obtained repeatedly and compared with the fit, less than 5% would be worse than this. Apart from one, they are all below $\chi^2 < 96$, which is the 5% significance level for a χ^2 distribution with 75 degrees of freedom (the red region). This indicates that all the fits are reasonable and statistically sound as being valid fits.

Another way of assessing the stability of the $Z \to \mu\mu$ measurement is to look at the

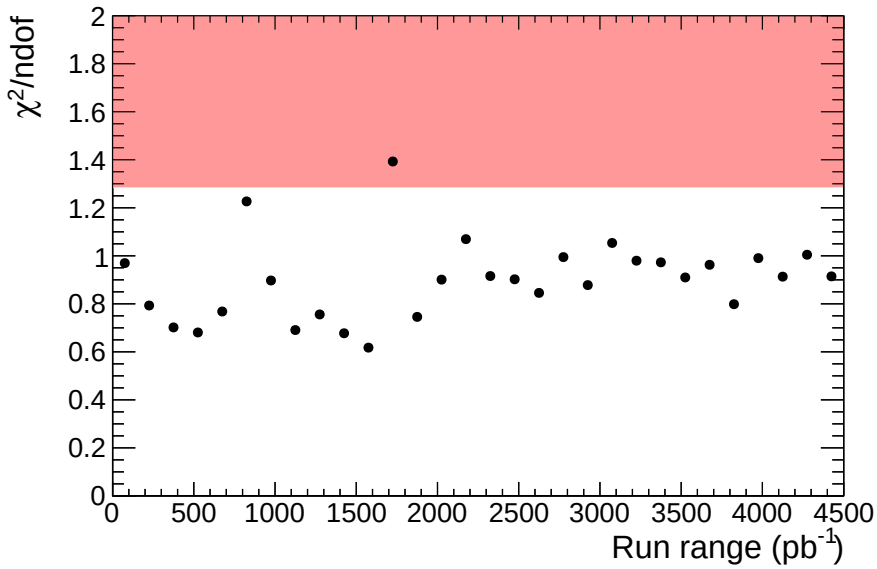

Figure 8.3: The χ^2/ndof of the simultaneous fit for each segment of time-ordered 150 pb^{-1}, as measured by the official Van der Meer scan calibrated HF system. The red region represents the 5% significance level of the fit.

overall efficiency ϵ of identifying the $Z \to \mu\mu$ decays over time. The overall efficiency is simply the total number of events we have in the mass window ($M \in (60, 120)$ GeV/c^2) in all five categories minus the fitted background in each category all divided by the efficiency-corrected yield $\mathcal{N}$. Once again we use the same 30 segments of 150 pb^{-1}, as measured by the official Van der Meer scan calibrated HF system. Figure 8.4 shows that the efficiency remains relatively stable at around $\epsilon \approx 0.97$. The slight variations are caused by the LHC's instantaneous luminosity not being constant throughout the data-taking season and this changes the efficiency (we investigate this in more detail in Section 8.4).

8.4 Stability with regards to Pileup

The Large Hardon Collider does not currently operate at the design luminosity of $\mathcal{L} = 10^{34}$ cm^{-2}s^{-1}, which would provide up to 25 pp collisions for every event that is read out by the detector. The phenomenon of multiple collisions being superimposed on a single events is known as pileup. There is also a proposed upgraded to the LHC, called the Super Large Hadron Collider. This proposal aims to increase the luminosity by a factor of 10, where pileup would be even more pronounced.

Pileup makes reconstruction much harder and subsequently the efficiency of recon-

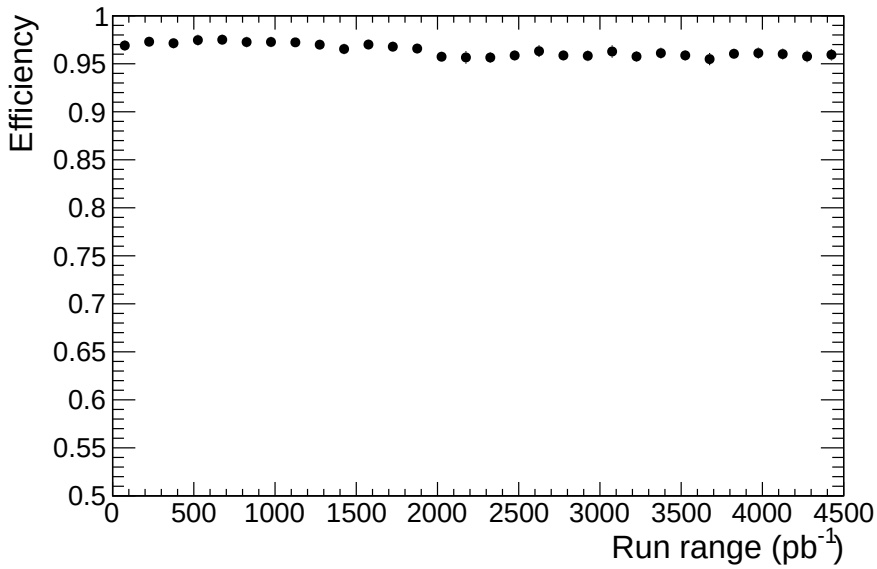

Figure 8.4: The overall efficiency of identifying $Z \to \mu\mu$ decays for each time-ordered segment of 150 pb^{-1}, as measured by the official Van der Meer scan calibrated HF system.

struction, ϵ, suffers accordingly. The decay particles of multiple collisions in the event causes a lot of hits in the inner tracker and energy deposits in the calorimeters. When the inner silicon tracker is too crowded with hits, there is not enough distance between each particles' trajectory and the hits start to overlap. This makes it very hard to work out which hits correspond to which decay particle and construct reliable tracks. Overlaps of energy deposits in the calorimeters also make identification of the decay particles hard. With so many decay tracks and deposits in the calorimeters and the inner silicon and outer muon trackers, it becomes increasingly hard to match them to each other too. All of this makes reconstruction more difficult and the chance of failure is increased, leading to a lower efficiency.

For the $Z \to \mu\mu$ measurement of integrated luminosity to be usable in the future, when the LHC increases its instantaneous luminosity towards the design specification and perhaps beyond, the measurement needs to be stable with regards to pileup too. The LHC does not always produce the same instantaneous luminosity. For example at the beginning of a fill it tends to have a higher instantaneous luminosity than at the end of a fill when the beam does not have as many protons in the bunches. We can use this variation in instantaneous luminosity to investigate the stability with regards to pileup.

We divide up the range of instantaneous luminosity into 30 segments. The size of these segments then vary so that the integrated luminosity of the collisions within

that instantaneous luminosity segment adds up to 150 pb^{-1}, as measured by the Van der Meer scan calibrated luminosity. The text file that is output by our analysis code (see Section 5.3) contains the mass of each event and the instantaneous luminosity of the bunch crossing. We use this to sort our events into the segments and create an invariant mass distribution histogram for each segment. We then run the fitter on each segment, using initial guess yields from Table 8.1 and the remaining initial parameters from Table 6.2.

As we did with the time-ordered segments, we look at plots of measured integrated luminosity, χ^2/ndof and overall efficiency. These are shown in Figure 8.5 through Figure 8.7. The alternating background grey shading shows the instantaneous luminosity segment ranges for each point.

Apart from the first instantaneous luminosity segment, the $Z \to \mu\mu$ measurement of integrated luminosity agrees well with the Van der Meer scan calibrated HF system to within the uncertainties. The $Z \to \mu\mu$ measurement does not vary much, staying in the same region of integrated luminosity; this shows that the measurement of integrated luminosity using $Z \to \mu\mu$ decays is stable with respect to pileup and can be continue to be used as the instantaneous luminosity increases at the LHC. Once again, the χ^2 plot shows us that the fits are good.

However, the first instantaneous luminosity segment ($0 < \mathcal{L}_{\text{BX}} < 0.66\ \mu\text{b}^{-1}\text{s}^{-1}$) does seem to be an anomaly. The range for this segment is much wider than all the other segments, because the LHC provides so few collisions with such a low instantaneous luminosity. This might cause significant errors in this segment due to the low statistics.

As we expected, the efficiency decreases as the instantaneous luminosity increases, because reconstruction becomes harder as pileup increases. However, it only decreases slowly in a seemingly linear fashion. If we extrapolate this and assume that it will continue to decrease at the same linear rate, we see that we can continue to use this $Z \to \mu\mu$ measurement of integrated luminosity even as the LHC instantaneous luminosity increases up to tenfold over its current instantaneous luminosity, as the efficiency will not be prohibitively low. The efficiency also decreases very smoothly as the instantaneous luminosity increases; this implies that the $Z \to \mu\mu$ measurement is very stable and consistent when repeated many times.

8.5 Cross-check with $Z \to ee$ Decays

A very similar integrated luminosity measurement was done using $Z \to ee$ decays on the same data [21]. Although the exact analysis differs, the principle of Equation (1.3) remains the same. As this is completely independent analysis that uses a different

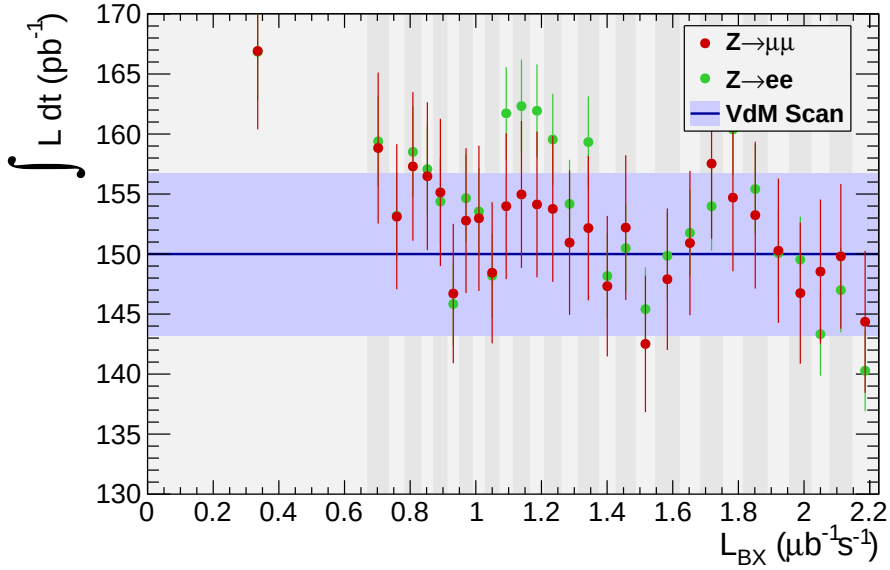

Figure 8.5: Total integrated luminosity for each instantaneous-luminosity-ordered segment of 150 pb^{-1}, as measured by the official Van der Meer scan calibrated HF system. Both the $Z \to \mu\mu$ measurement and the Van der Meer scan calibrated measurement are shown with their 1σ uncertainties.

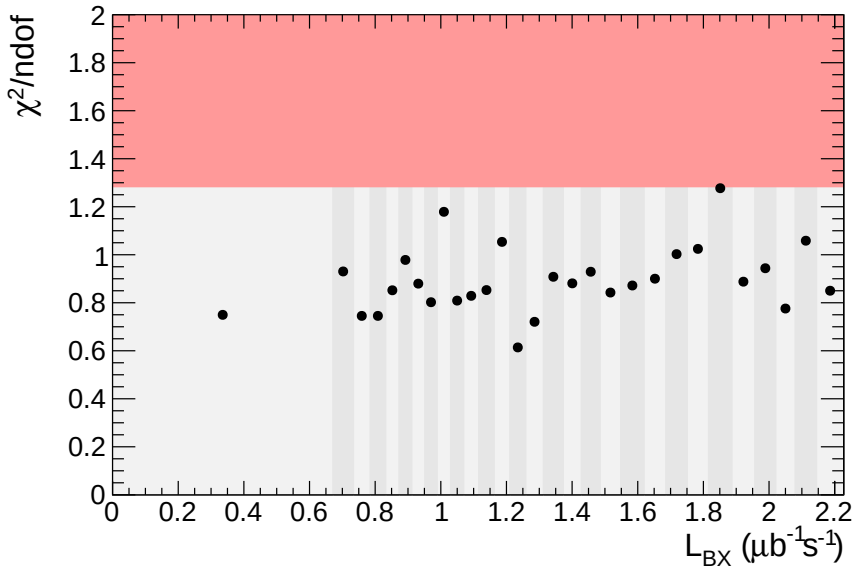

Figure 8.6: The χ^2/ndof of the simultaneous fit for each instantaneous-luminosity-ordered segment of 150 pb^{-1}, as measured by the official Van der Meer scan calibrated HF system. The red region represents the 5% significance level of the fit.

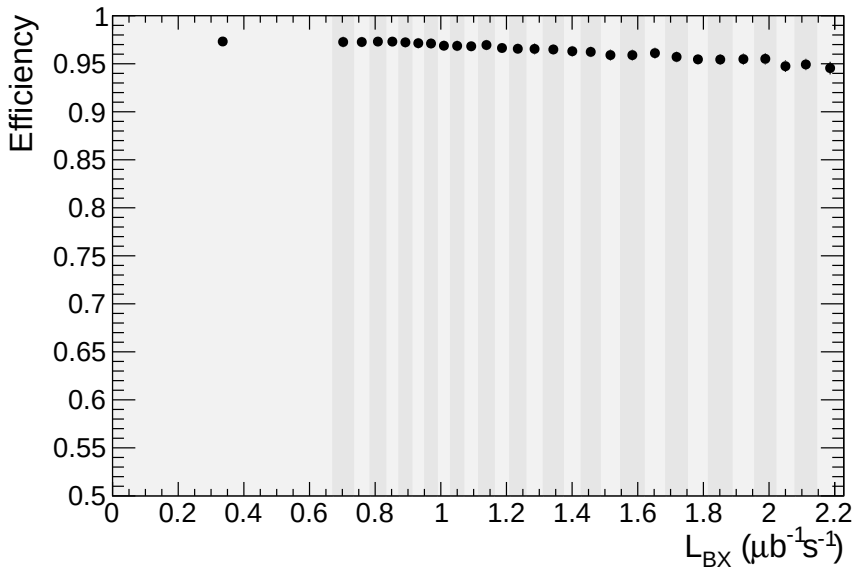

Figure 8.7: The overall efficiency of identifying $Z \to \mu\mu$ decays for each instantaneous-luminosity-ordered segment of 150 pb^{-1}, as measured by the official Van der Meer scan calibrated HF system.

physics channel (electron identification is done in a different way), it is a worthwhile cross-check to compare our $Z \to \mu\mu$ measurement of integrated luminosity with their $Z \to ee$ measurement.

Figure 8.2 also shows the integrated luminosity measurement using $Z \to ee$ decays of the 30 time-ordered 150 pb^{-1} segments, on top of the $Z \to \mu\mu$ based measurement and the Van der Meer scan calibrated measurement. As it is a little hard to see the datapoints and error bars for both the $Z \to ee$ measurement and the $Z \to \mu\mu$ measurement on Figure 8.2, we plot the ratio of the two measurements in Figure 8.8. Every data point on this ratio plot is around unity, and, if we include the error bars, we find that almost every single data point demonstrates that the measurement using $Z \to \mu\mu$ decays agrees with its $Z \to ee$ counterpart to within the uncertainties of the measurement. Along with the Van der Meer scan calibrated HF system, this provides yet another verification that the $Z \to \mu\mu$ measurement of total integrated luminosity is accurate.

We also compared the instantaneous-luminosity-ordered $Z \to \mu\mu$ measurement with the $Z \to \mu\mu$ in a similar manner in Figure 8.5 and Figure 8.9. We come to the same conclusion as with the time-ordered segments: all three independent methods agree with each other to within the uncertainties and together these show that the the $Z \to \mu\mu$ measurement of total integrated luminosity is correct.

While the $Z \to ee$ measurement provides a useful cross-check to our $Z \to \mu\mu$

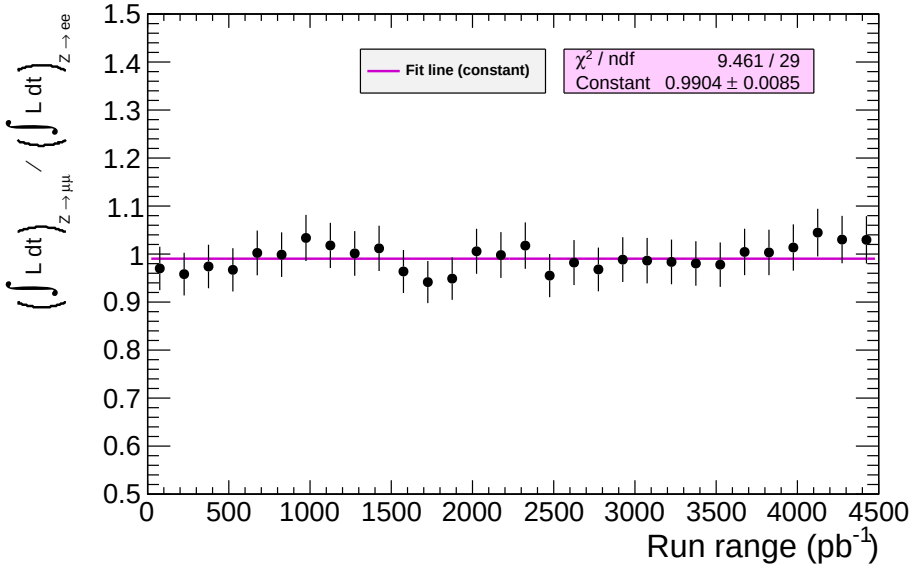

Figure 8.8: The ratio of the integrated luminosity measurement performed using $Z \to \mu\mu$ decays to that using $Z \to ee$ decays for each of the 30 time-ordered segments. The best fit to the ratio using a constant is calculated and drawn on top as a line.

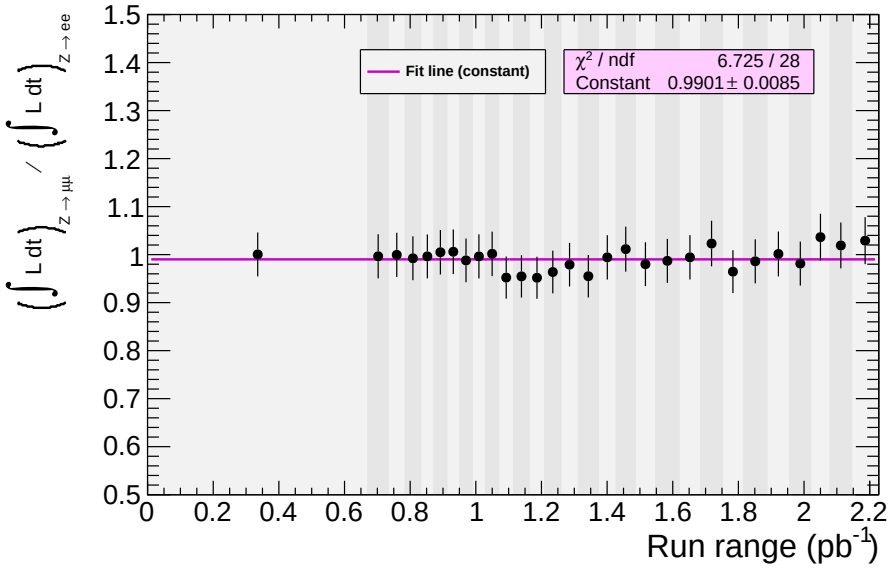

Figure 8.9: The ratio of the integrated luminosity measurement performed using $Z \to \mu\mu$ decays to that using $Z \to ee$ decays for each of the 30 instanteneous-luminosity-ordered segments. The best fit to the ratio using a constant is calculated and drawn on top as a line.

measurement, there are several advantages that the $Z \to \mu\mu$ physics channel has over the $Z \to ee$ channel:

- Over the course of the 2011 data, the $Z \to ee$ efficiency fluctuates significantly more than $Z \to \mu\mu$ efficiency. This indicates that the measurement of integrated luminosity using $Z \to \mu\mu$ decays may be more desirable as it is more stable and consistent.

- As instantaneous luminosity increases, although both the $Z \to ee$ and the $Z \to \mu\mu$ measurements lose efficiency, the $Z \to \mu\mu$ method loses efficiency much less. As the instantaneous luminosity increases further at the LHC, the $Z \to ee$ method may no longer be possible as the efficiency might become too low.

Chapter 9

Conclusions

We have demonstrated that with the 2011 data we are able to divide it into segments of 150 pb^{-1} and measure the absolute integrated luminosity using $Z \to \mu\mu$ decays to an accuracy of 3.4%. Not only do these measurements agree with the official HF luminosity calibrated by Van der Meer separation scans, but they also achieve a lower uncertainty. Our measurements have also been cross-checked using an independent physics candle method utilising $Z \to ee$ and found to be consistent. We have also shown that our measurements are stable and consistent both over time and with respect to pileup.

As a result, we recommend that the LHC use $Z \to \mu\mu$ decays to measure the absolute integrated luminosity on segments of data that are roughly 100 pb^{-1} sized. At design luminosity of $\mathcal{L} = 10^{-34}$ $\text{cm}^{-2}\text{s}^{-1}$, segments of this size are produced every 3 hours and $Z \to \mu\mu$ decays could provide a near-realtime integrated luminosity measurement. Although the LHC has not currently reached the design luminosity, segments of this size could still be produced every day. Changes in efficiency could also be used to check the stability of the detector itself on a near-realtime basis.

Measuring integrated luminosity using $Z \to \mu\mu$ decays is currently limited by parton distribution function systematic uncertainty. As these improve in the future, this luminosity measurement could achieve an accuracy of 1-2%, which has never been achieved before from a physics candle in a hadron collider.

The integrated luminosity underpins every cross-section measurement made at the LHC and therefore is an important measurement. A $Z \to \mu\mu$ decay based measurement, in conjunction with a Van der Meer scan calibrated HF measurement and a $Z \to ee$ decay based measurement, will provide a reliable and verified measurement of the total absolute integrated luminosity using a standard physics candle, to a level of precision not previously achieved at a hadron collider.

References

[1] J. Werner, "Measurement of the Inclusive $Z \to ee$ production cross section in proton-proton collisions at $\sqrt{s} = 7$ TeV and $Z \to ee$ decays as standard candles for luminosity at the Large Hadron Collider". PhD thesis, Princeton University, November, 2011.

[2] K. Nakamura et al. (Particle Data Group), "The Review of Particle Physics", *J. Phys. G* **37** (2010) 075021.

[3] R. Gavin, Y. Li, F. Petriello et al., "FEWZ 2.0: A code for hadronic Z production at next-to-next-to-leading order", *Comput. Phys. Commun.* **182** (2011) 2388–2403, `arXiv:1011.3540`. `doi:10.1016/j.cpc.2011.06.008`.

[4] A. Martin, W. Stirling, R. Thorne et al., "Parton distributions for the LHC", *Eur.Phys.J.* **C63** (2009) 189–285, `arXiv:0901.0002`. `doi:10.1140/epjc/s10052-009-1072-5`.

[5] CMS Collaboration, "Measurement of the Inclusive W and Z Production Cross Sections in pp Collisions at $\sqrt{s} = 7$ TeV", *JHEP* **1110** (2011) 132, `arXiv:1107.4789`. `doi:10.1007/JHEP10(2011)132`.

[6] CMS Collaboration, "How CMS detects particles". `http://cms.web.cern.ch/news/how-cms-detects-particles`. Accessed: 27/04/2012.

[7] N. Adam, V. Halyo, A. Hunt, J. Jones, D. Marlow, J. Werner, Z. Xie,W. Badgett, Y. Guo, L. Lueking, K. Maeshima, S. Kosyakov,D. Baden, and T. Grassi, "The CMS Luminosity Readout System",. CMS IN-2007/052.

[8] CMS Collaboration, "Measurement of CMS Luminosity", *CMS Physics Analysis Summary* **EWK-10-004** (2010).

[9] S. van der Meer, "Calibration of the effective beam height in the ISR. oai:cds.cern.ch:296752", Technical Report CERN-ISR-PO-68-31, CERN, Geneva, 1968.

[10] CMS Collaboration, "Absolute Calibration of Luminosity Measurement at CMS: Summer 2011 Update", *CMS Physics Analysis Summary* **EWK-11-001** (2011).

[11] CMS Collaboration, "Notes on Addition to `lumicalc.py` for 2011 Calibration Corrections: December 2011 Update". `https://twiki.cern.ch/twiki/pub/CMS/LumiCalc/LumiCorrection_v2.1.pdf`. Accessed: 27/04/2012.

[12] CMS Collaboration, "Absolute Calibration of Luminosity Measurement at CMS: Winter 2012 Update", *CMS Physics Analysis Summary* **SMP-12-008,** (2012).

[13] S. Alioli, P. Nason, C. Oleari et al., "NLO vector-boson production matched with shower in POWHEG", *JHEP* **0807** (2008) 060, `arXiv:0805.4802`. `doi:10.1088/1126-6708/2008/07/060`.

[14] T. Sjostrand, S. Mrenna, and P. Z. Skands, "PYTHIA 6.4 Physics and Manual", *JHEP* **0605** (2006) 026, `arXiv:hep-ph/0603175`. `doi:10.1088/1126-6708/2006/05/026`.

[15] H.-L. Lai et al., "New parton distributions for collider physics", *Phys. Rev.* **D82** (2010) 074024, `arXiv:1007.2241`. `doi:10.1103/PhysRevD.82.074024`.

[16] D. Kovalskyi, M. Tadel, A. Mrak-Tadel et al., "Fireworks: A physics event display for CMS", *Journal of Physics: Conference Series* **219** (2010), no. 3, 032014.

[17] CMS Collaboration, "ZMuMu source code". `http://cmssw.cvs.cern.ch/cgi-bin/cmssw.cgi/CMSSW/ElectroWeakAnalysis/ZMuMu/`. Accessed: 27/04/2012.

[18] I. Antcheva et al., "ROOT – A C++ Framework for Petabyte Data Storage, Statistical Analysis and Visualization", *Comp. Phys. Comm.* **180** (2009), no. 12, 2499–2512.

[19] M. De Gruttola, A. De Cosa, F. Fabozzia and L. Lista, "Determination of the $pp \to ZX \to \mu^+\mu X$ inclusive cross section with a simultaneous fit of Z yield, muon reconstruction efficiencies and trigger efficiency with the first 2.9 pb^1 of 7 TeV collision data", *CMS Analysis Notes* **AN-2010-345** (2010).

[20] CMS Collaboration, "The official CMS Luminosity Calculation". `https://twiki.cern.ch/twiki/bin/view/CMS/LumiCalc`. Accessed: 27/04/2012.

[21] M. de Gruttola, T. Lou, V. Halyo, J. Werner, M. Wu, "Inclusive $Z \to ll$ Decays as Standard Cnadles for Luminosity at the LHC in 2011", *CMS Standard Model Physics Group Meeting* (2012). CADI-EWK-11-018.

Statement of Academic Integrity

This paper represents my own work in accordance with University regulations.